IEEE Access
Multidisciplinary | Rapid Review | Open Access Journal

Date of publication xxxx 00, 2023, date of current version xxxx 00, 2023.

Digital Object Identifier 10.1109/ACCESS.2023.Doi Number

Low-Cost Thermal-Infrared 'THz-Torch' Spectroscopy

SALEH KOMIES[1], JINGYE SUN[1,2], CHRIS HODGES[3], STEPHEN A. LYNCH[3] (Senior Member, IEEE), JONATHAN S. WATSON [4] and STEPAN LUCYSZYN[1], (Fellow, IEEE)

[1]Department of Electrical and Electronic Engineering, Imperial College London, London SW7 2AZ, U.K.
[2]School of Electronic and Information Engineering, Beijing Jiaotong University, Beijing, China.
[3]School of Physics and Astronomy, Cardiff University, Cardiff, CF24 3AA, U.K.
[4]Department of Earth Science and Engineering, Imperial College London, London, SW7 2BX, U.K.

Corresponding author: Stepan Lucyszyn (s.lucyszyn@imperial.ac.uk).

This work was supported by ARAMCO Overseas Company Ltd.

ABSTRACT The low-cost thermal infrared 'THz-Torch' concept (referred to here as 'THz-T') was first introduced over a decade ago, and since then the associated 'over the THz horizon' thermal infrared (10-100 THz) implementation technologies have continued to advance. While short range secure wireless communications links have received a great deal of attention, material spectroscopy has only briefly been introduced in a short conference abstract. Here, for the first time, we explore in depth the basic concepts behind THz-T spectroscopy. Moreover, when compared to the unvalidated results within our previous work, we demonstrate an enhanced experimental THz-T spectrometer. A detailed thermal noise power link budget model for both the transmission and reflection modes of operation have been undertaken and independently validated. As a proof of principle, a diverse array of different material types has been characterized. This includes glass sheets, semiconductor wafers, ceramic plate, plastic tape, plastic sheets, as well as polymer and cotton paper banknotes. THz-T technology has the advantages of hardware simplicity and low cost non-destructive testing for ubiquitous applications.

INDEX TERMS Terahertz, thermal infrared, blackbody radiation, spectroscopy, FTIR, THz TDS, transmittance, reflectance, absorptance, material characterization.

I. INTRODUCTION

With conventional molecular spectroscopy within the broader terahertz (THz) spectrum (0.1 to 10 THz), a unique frequency-domain fingerprint is created for a sample under test (e.g., solid, liquid, gas) [1]. Spectral absorption lines can be detected with the use of THz time-domain spectroscopy (THz TDS), for the non-destructive and non-invasive identification of chemical and biological samples. However, commercial THz TDS systems [2]-[6] and infrared (IR) spectrometers (0.3 to 750 THz) [7]-[10] are very expensive.

THz TDS allow users to generate both magnitude and phase measurements and is the spectroscopists method of choice; not least because coherent pump-probe detection offers for an extremely high signal-to-noise ratio (SNR), with excellent dynamic range [11]. Unfortunately, (sub-)picosecond pulsed laser-based systems are very costly, especially when used for just the occasional characterization of material samples. A lower-cost solution is to use either a dedicated frequency-domain continuous wave (CW)-THz or low SNR space-domain Fourier transform infrared (FTIR) spectrometer. For the non-spectroscopists, the use of existing general purpose sub-THz frequency-domain vector network analysers would be the preferred option for material characterization; not least because of their extremely high SNR and sub-megahertz frequency resolution. As with CW-THz and FTIR spectroscopy, until recently, there has been insufficient information from conventional reflection-transmission mode measurements for extracting complex dielectric properties with (semi-)transparent samples [11].

In 2011, the 'THz Torch' concept was introduced to exploit low-cost techniques within the thermal infrared (TIR) (*ca.* 10 to 100 THz) [12]-[19]. Within this part of the frequency spectrum, coherent sources and detectors are very expensive. In contrast, very low-cost thermal emitters (e.g., ubiquitous incandescent light bulbs heaters [14]) can be used as an incoherent noise carrier generator, which can be easily modulated using ON-OFF keying to send data. Moreover, very low-cost detectors can be implemented using a pyroelectric infrared (PIR) and Golay cell sensors (e.g., ubiquitous motion sensors). Many advances

have been made over the past decade in wireless communications applications [12]-[19], most recently in 2020 with the use of enhanced cognitive demodulation [18] with artificial intelligence [19].

To date, THz-T spectroscopy has received little attention. From an extensive literature search, the only example is the characterization of banknotes in our 2015 three-page conference abstract [20]. The fundamental concept behind THz-T spectroscopy is not to perform accurate spectroscopy on a material under test (MUT), but to simply identify the MUT from a database of other pre-characterized materials using very sparse discrete frequency spectrum sampling. Inherently, sparse frequency spectrum sampling is unable to resolve fine spectral features. As a result, unlike traditional spectroscopy that identifies a MUT from its spectral absorption line signature, THz-T spectroscopy is aimed at the smooth parts of the spectral response that are away from absorption lines. Therefore, identification relies on the MUT to have few absorption lines (i.e., relatively smooth spectral features) within the thermal infrared spectral range of interest.

A commercial FTIR spectrometer is generally available in the transmission mode, unless incorporating external interchangeable sampling accessories to implement different reflection modes (e.g., 45° specular reflection and diffuse reflection). In contrast, the THz-T spectrometer offers a cost-effective solution and has the advantage of being able to operate in both transmission and reflection modes with the same hardware (e.g., source and detector) and with fewer additional optical components. This lends itself to non-destructive testing (NDT) in the field.

This paper benchmarks the performance of the THz-T spectrometer against commercial high-resolution spectrometers, validating both transmission and reflection modes with a diverse array of different materials. Here, we include glass sheets (fused quartz, fused silica and borosilicate), semiconductor wafers (low-resistivity silicon and semi-insulating gallium arsenide (GaAs)), ceramic plate (alumina) and plastic tape (polyimide), polymer sheets (polytetrafluoroethylene (PTFE) and polypropylene (PP)), polymer banknotes (British Pound (GBP, £) and Canadian Dollar (CAD, $)) and cotton paper banknotes (GBP and Chinese Yuan (CNY, ¥)).

The paper is structured as follows: Section II, provides a brief, non-exhaustive literature review of FTIR spectrometer techniques and applications. Within this context, we greatly expand on our first proof-of-principle THz-T spectrometer [20]. In Section III, an enhanced and more compact THz-T spectrometer is presented for the first time. In Section IV, this experimental prototype THz-T spectrometer demonstrator is discussed in more. In Section V, a detailed predictive thermal noise power link-budget model is included and the practical limitations of this technology are discussed. In Section VI, the performance of the THz-T spectrometer is benchmarked against commercial high-resolution spectrometers. Finally, in Section VII, a discussion and summary is given of the findings from our experiments with the THz-T spectrometer, as well as a low-cost justification for our system.

II. BACKGROUND

FTIR spectroscopy has been widely used to obtain a sample's infrared spectra (e.g., transmittance, reflectance and absorptance) [1]. For examples, identifying; (i) gases and their concentration in environmental, medical, industrial, security and defence applications [21]; (ii) minerals [22]; (iii) molecules in food and drug tests [23]; (iv) remote sensing over long distances for open path gas analysis [24]; and near-field spectromicroscopy [25]-[26].

With IR spectroscopy, the frequency spectrum is divided-up into two main regions: 'complicated' fingerprint region (12 to ~45 THz) and 'cleaner' diagnostic region (~45 to 120 THz). The former region displays the effects of mostly single covalent bonds that have stretching and bending vibrations, which can identify specific molecules. The latter region displays the effects of mostly double and triple covalent bonds that have the stretching vibration, which can identify molecule bonds with their functional groups [27].

Commercial FTIR spectrometers [7]-[10] and FTIR microscopy [28]-[32] have different spectral range, spectral resolution, sources, detectors, accessories and optical components. For example, the typical Nicolet™ iS50 FTIR spectrometer, from Thermo Fisher Scientific [7], has a spectral range between 0.45 to 809 THz, with a spectral resolution of 2.7 GHz. It utilises multiple source and detector options. Within the TIR spectral range, it utilizes a Polaris long-life source, a deuterated L-alanine doped triglycene sulphate (DLaTGS) detector, potassium bromide (KBr) lenses and KBr beam-splitter; the hygroscopic KBr components require additional environmental considerations to avoid absorption of moisture and other contaminants.

Most modern commercial FTIR spectrometers employ Globar (silicon carbide rod) mid-infrared thermal sources that radiate into an interferometer. These create a high resolution interferogram from the detector; this corresponds to a plot of optical path difference versus power intensity. A Fourier transform (FT) is then applied to the interferogram, in order to produce a transmittance (and absorbance, which is the inverse of transmittance and should not be confused with absorptance) spectrum, as a function of wavenumber. The required hardware (e.g., sources, detectors, electronically-scanned micro-positioners, vacuum/gas-sealed or desiccated MUT compartment, optical filters, helium-neon (HeNe) positioning laser, etc.). As a result, this high-performance commercial solution does not easily lend itself to being affordable or portable. In contrast, there is growing interest (e.g., within the low-end manufacturing sector), in the cost-performance application space that can achieve minimal performance at lower cost.

The first reported THz-T spectrometer [20], exploits 16 discrete spectral data points, between 20 to 80 THz. This fundamentally utilizes engineered blackbody radiation by separating thermally-generated power into pre-defined spectrum sampling filter (SSF) bandwidths.

The previously reported hardware implementation was only used to characterize paper and plastic banknotes [20]. Most banknotes are still made from 100 µm thick cotton paper, which is sometimes mixed with linen, abaca or other textile

fibers. Both the older GBP and current CNY banknotes are paper-based and have a 1 or 2 mm wide metallic strip for the £20 and ¥100 banknotes, respectively. The older £20 banknote also has a metallic hologram, to further enhance its counterfeit resilience. In contrast, the $10 banknote is made from a 100 μm thick polymer (the exact nature of this material is confidential and so untraceable), having a transparent window and metallic holographic regions. Across the 20 to 80 THz spectral region, the paper-based banknotes exhibit very high absorptance (>95% [20]) with both low reflectance and transmittance (<3% [20]), away from the metallic holograms/strips; while the polymer-based banknotes have complex absorptance and transmittance spectral signatures, with low reflectance (<10% [20]), away from the metallic holograms. It is important to note that none of these early THz-T measurements were verified by independent modeling and measurements.

III. SYSTEM DESIGN OVERVIEW

A. BASIC ARCHITECTURE

The THz-T spectrometer concept relies on all the critical commercial-off-the-shelf (COTS) components (TIR emitter, filters, chopper, lenses and detector) to be simple and low cost for NDT and non-invasive material characterization applications. Figures 1(a) and 1(b) show illustrations of the system setups for the transmission and reflection modes of operation, respectively.

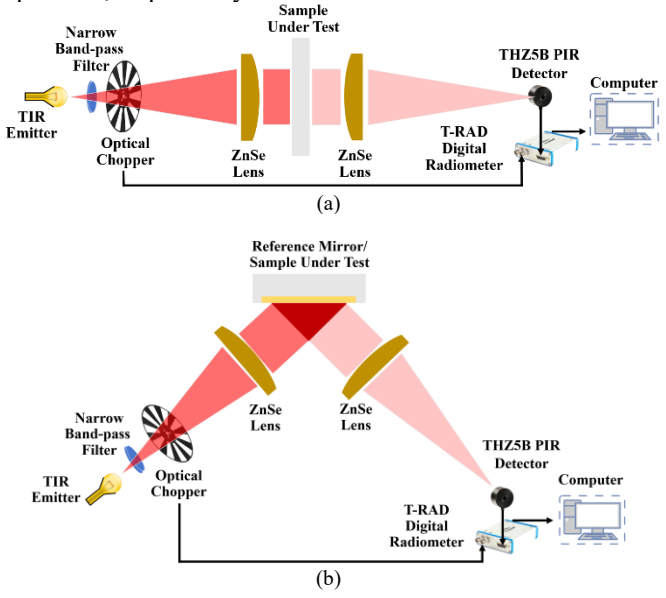

FIGURE 1. Simplified illustrations of the THz-T spectrometer: (a) transmission mode; and (b) reflection mode.

The previously reported architecture [20] employs (COTS) components: (i) Intex Inc. TIR emitter, having an 80% emissivity over a spectral range from 15 to 300 THz [33]; (ii) sixteen pairs of Northumbria Optical Coating (NOC) Ltd substrate optical narrow band-pass filters, nominally used for gas and vapor analysis [34]; (iii) Bentham optical chopper and control module [35], for lock-in amplifier radiometer measurements operating at a chopping frequency of 25 Hz; (iv) 5-slot mechanical chopper disc; (v) pair of Korth Kristalle Inc. KBr plano-convex lenses, used to minimize radiation spreading loss to collimate and focus beams [36]; (vi) Gentec-EO Inc. THZ5B PIR detector [37]; (vii) microprocessor-based digital Gentec-EO Inc. terahertz radiometer (T-Rad), which includes software that simplifies the process of configuring the radiometer for THz measurements [38]; and (viii) Thorlabs Inc. enhanced gold coated mirror, having 99.5% reflectance [39], used for the reference path in the reflection mode only.

Here, we propose an enhanced experimental THz-T spectrometer, having a similar basic architecture for both transmission and reflection modes, with COTS components, but with significant enhancements. For example: (i) removing matched spectrum sampling filter pairs (one at the TIR emitter and the other at the PIR detector), keeping just one at the TIR emitter – simplifying complexity and cost, while also improving the received signal strength at the detector (between 0.71 and 2.17 dB, depending on the filter); (ii) increasing the number of SSFs, from 16 to 21, extending the upper spectral range of interest (from 80 to 100 THz). The new filter family [34], [40] has a band-average transmittance ranging between 61% and 85%, while the fractional bandwidth of the filters varies between 0.8% and 4.6%; (iii) a new Scitec Instruments Ltd 10-slot mechanical chopper disc (with 51 mm radius and 0.5 mm thickness), for chopping frequencies between 25 and 1,000 Hz with ±1° phase jitter, to minimise wobble [41]; (iv) replacing the pair of 1.5 cm diameter KBr plano-convex lenses with 2.54 cm diameter zinc selenide (ZnSe) lenses [42] – the wider spectral response of the higher transmittance KBr lenses, within the TIR range (~90% transmittance from 15 to 750 THz), is adversely affected by moisture in the atmosphere and so they must be stored in a desiccator between measurements. The anti-reflection coated ZnSe lens has a narrower spectral range (>92% average transmittance from 21 to 150 THz) [42]; and (v) employ bespoke 3-D printed components (e.g., housings, mounts and sample holder) provide effortless assembly and alignment on the optical bench – offering the prospect of low-cost 'plug and play' implementations with good alignment [43]-[44].

B. TIR EMITTER

Commercial TIR emitters have been used as the thermal source in our THz-T systems, for both wireless communications links [18]-[19] and spectroscopy applications [20]. The TIR emitter INTX 17-0900 has been found to be an efficient replacement for the original incandescent light bulbs [12]-[16]. Planck's law calculates the spectral radiance emitted from an ideal blackbody emitter $I_{BB}(T_{BB})$, as a function of absolute blackbody temperature T_{BB}, which is assumed here to be the physical temperature $T = T_{BB}$. Now, Planck's law can be expressed as a function of frequency (f), wavelength (λ) or wavenumber. Here, the frequency-dependent spectral radiance is used, given by:

$$I_{BB}(f, T_{BB}) = \frac{2hf^3}{c^2} \cdot \frac{1}{e^{hf/k_B T} - 1} \quad [\mathrm{W \cdot sr^{-1} \cdot m^{-2} \cdot Hz^{-1}}] \quad (1)$$

where, h = 6.6261×10^{-34} J·s is the Planck constant, k_B = 1.3806×10^{-23} J/s is the Boltzmann constant and c is the speed of light in a vacuum.

The frequency of the peak in spectral radiance for an ideal blackbody is found by differentiating (1) with respect to f. This will result in Wien's displacement law, with its frequency-dependent form given by:

$$f_{peak} = \frac{\alpha k_B}{h} \cdot T \text{ [Hz]} \simeq 58.789 \cdot T \text{ [GHz]} \quad (2)$$

where, f_{peak} is the peak frequency [GHz] and $\alpha \simeq 2.8214$ is the transcendental equation coefficient. Substituting $T = T_{BB}$ = 1,023 K in (2) yields a value of $f_{peak} \simeq 60.14$ THz. Note that, the wavelength-dependent form of Planck's law has an associated Wien's displacement law that yields a wavelength of the peak in spectral radiance $\lambda_{peak} = b/T = 3.01\ \mu\text{m} \neq c/f_{peak}$, where b is the Wien's displacement constant [45].

The radiance (or total radiant power) emitted by the perfect blackbody can be found by integrating (1) over all frequencies:

$$I_{BB}(T) = \int_0^\infty \frac{2hf^3}{c^2} \frac{1}{e^{hf/k_BT}-1} \cdot df = \frac{2\pi^4 {k_B}^4}{15h^3c^2} \cdot T^4 \quad [\text{W}\cdot\text{sr}^{-1}\cdot\text{m}^{-2}] \quad (3)$$

To calculate the total radiated power per unit area, (3) is integrated with respect to the solid angle Ω over the hemisphere into which the surface of the source radiates. This is referred to as the radiant emittance (or radiant exitance [44]). Ideal blackbody sources are considered Lambertian because of its isotropic radiance (i.e., they radiate energy equally in all direction, regardless of the observation angle). The response follows Lambert's cosine law of reflection. This states that the radiant intensity of light reflected from a Lambertian surface is proportional to the cosine of the angle between the surface normal and the observation direction. Thus, for a Lambertian source, the radiated power per unit area is given by the Stefan-Boltzmann law:

$$\begin{aligned} P_s(T) &= I_{BB}(T) \int_0^{2\pi} \cos\theta \cdot d\Omega \\ &= I_{BB}(T) \int_0^{2\pi} \cdot d\varphi \int_0^{\frac{\pi}{2}} \cos\theta \sin\theta \cdot d\theta \\ &= \pi I_{BB}(T) = \sigma \cdot T^4 \quad [\text{W}\cdot\text{m}^{-2}] \end{aligned} \quad (4)$$

where, $$\sigma = \frac{2\pi^5 {k_B}^4}{15h^3c^2} = 5.6704 \times 10^{-8} \quad [\text{W}\cdot\text{m}^{-2}\cdot\text{K}^{-4}] \quad (5)$$

and Ω is the solid angle; θ and φ are the respective zenith and azimuth angles in spherical coordinates, satisfying $d\Omega = sin\theta \cdot d\theta \cdot d\varphi$; and σ is the Stefan-Boltzmann constant. The $cos\theta$ term is due to the Lambertian nature of the thermal emitter.

With regards to our TIR emitter, which can be approximated as a radiator having an absolute temperature T and emissivity $\mathcal{E}(f,T)$, the spectral radiance $I_e(f,T)$ can be calculated from:

$$I_e(f,T) = \mathcal{E}(f,T) \cdot I_{BB}(f,T) \quad [\text{W}\cdot\text{sr}^{-1}\cdot\text{m}^{-2}\cdot\text{Hz}^{-1}] \quad (6)$$

The typical spectral range for the INTX 17-0900 is 15 to 300 THz [33], while the operational temperature ranges from 878 to 1,023 K, depending on the bias level. With the previous line-of-sight communications link applications, in the steady state, the INTX 17-0900 emitter was biased with input direct current (DC) power P_{input} = 897.8 mW, to achieve its maximum rated temperature of T = 1,023 K [33], required for optimal SNR [18]-[19]. However, for our spectroscopy demonstrator, the regulated voltage supply to the TIR emitter is set to 6.4 V, drawing a steady-state current of 0.11 A, giving P_{input} = 704 mW; ensuring a longer lifetime of operation for the emitter, with expected T = 964 K. In practice, the emissivity of the TIR emitter, within our frequency and temperature ranges of interest, is effectively constant with $\mathcal{E}(f,T) \to \mathcal{E} = 0.8$ [33].

Our TIR emitter does not radiate over a sphere (unlike a perfect isotropic thermal source). It has a heated membrane film, which radiates over a half-space. As a result, the power spectral density p_e for our TIR emitter is given by:

$$\begin{aligned} p_e(f,T) &= A_e I_e(f,T) \int_0^{2\pi} \cos\theta \cdot d\Omega \\ &= \pi A_e I_e(f,T) \quad [\text{W}\cdot\text{Hz}^{-1}] \end{aligned} \quad (7)$$

where, the effective area of the TIR emitter's heated membrane film A_e = 2.89 mm^2, given the 1.7 mm × 1.7 mm dimensions of the heater's membrane. By integrating (7), over the TIR emitter's frequency of operation, the radiated power is given by:

$$P_e(T) = \int_{f_1}^{f_2} p_e(f,T) \cdot df \quad [\text{W}] \quad (8)$$

where, the 50% cut-on and cut-off frequencies for the TIR emitter are f_1 and f_2, respectively.

Using (6) and (7), Fig. 2 shows the calculated spectral radiance $I_e(f,T)$ and power spectral density, respectively, as a function of frequency. The former indicates the extreme temperature range of operation, while the latter is for the expected operational temperature.

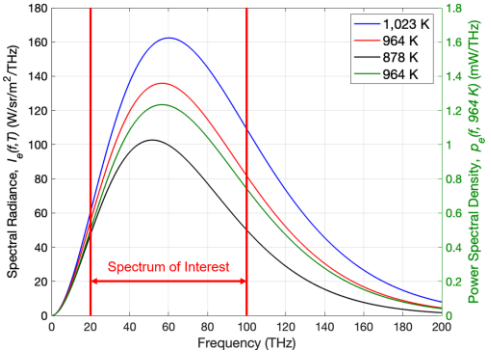

FIGURE 2. Calculated spectral radiance for the TIR emitter (INTX 17-0900) operating at different temperatures, and theoretical emitted radiated power at T = 964 K.

Substituting T = 964 K in (2) yields $f_{peak} \simeq 56.67$ THz, which indicates the maximum spectral radiance for our TIR emitter, based on the input DC power P_{input} = 704 mW.

Photographs of the internal structure of our TIR emitter (INTX 17-0900), having TO-39 packaging without and with reflector, are shown in Figs. 3(a) and 3(b), respectively. An illustration of the TIR power dissipation mechanisms is shown in Fig. 3(c).

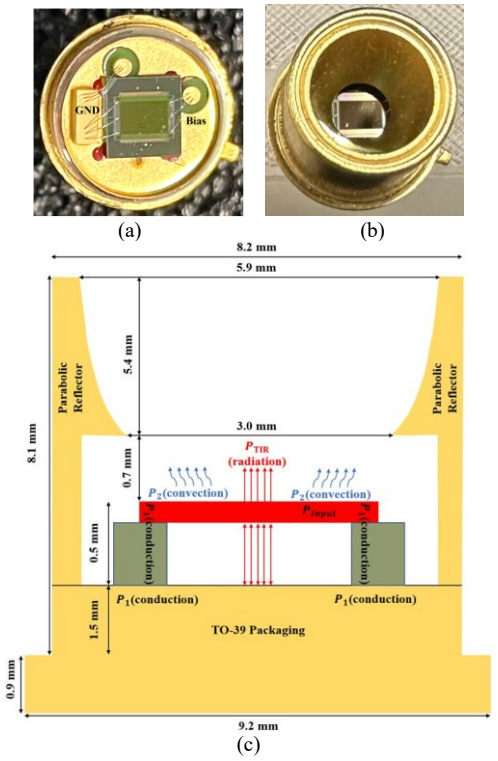

FIGURE 3. TIR emitter (INTX 17-0900): (a) plan-view photograph of TO-39 packaging without reflector; (b) perspective-view photograph with reflector; and (c) side-view illustration of power dissipation (not to scale).

From the TIR emitter, according to our previous analysis, the desired radiated power $P_e(T)$ relies on four parameters: spectral bandwidth, temperature, emissivity and size. With reference to Fig. 3(c), P_{Input} is dissipated through three main mechanisms, represented by the following principle of conservation of energy:

$$P_{Input} = P_e + P_1 + P_2 \tag{9}$$

where, P_1 is wasted power dissipated in the TIR emitter's silicon substrate (via thermal conduction), which includes backside radiation path losses; and P_2 is wasted power dissipated in air (via thermal convection). The quoted typical thermal power link budget for the INTX 17-0900 is represented in Table 1 [32]. It can be seen that this thermal emitter only has 16% power conversion efficiency (from input DC to output radiated TIR). With our scenario, given P_{input} = 704 mW, and the 16% conversion efficiency, T = 964 K is found using (4) to (9).

TABLE 1. Approximate thermal power link budget for the TIR emitter (INTX 17-0900) († T = 1,023 K [33]; ↓ T = 964 K).

Category	Proportion† (%)	Power↓ (mW)
Radiated, P_e	16	113
Conducted, P_1	24	169
Convected, P_2	60	422
Input DC, P_{input}	100	704

With reference to Fig. 3, it can be deduced that a significant amount of energy is wasted at the backside of the TIR emitter, as it is not projected towards the detector's field of view. This wasted energy is lumped together as a conduction loss in our calculations; represented by P_1.

With its flat surface, the radiation emitted has an angular distribution that follows a cosine function, with its peak at normal incidence, as shown in Fig. 4. In addition, the TIR emitter has a parabolic reflector that confines the radiated energy within a tighter solid angle; minimizing spreading loss. The angular distribution of the TIR emitter with a parabolic reflector, at a distance of 100 mm from the membrane surface, is also shown in Fig. 4.

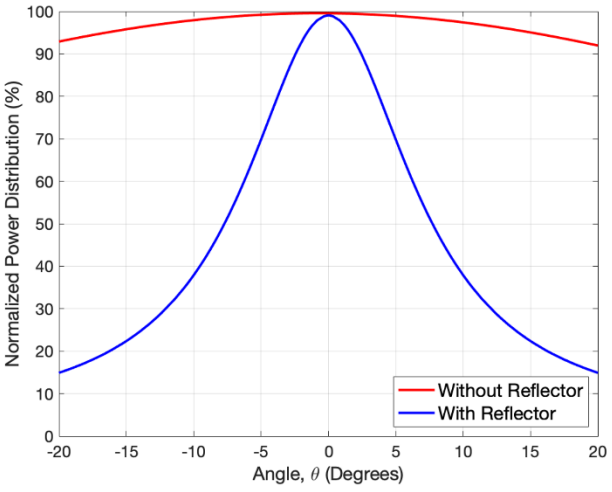

FIGURE 4. Two-sigma angular distribution of TIR radiation for the TIR emitter (INTX 17-0900), with a parabolic reflector, at a distance of 100 mm from the membrane surface [33].

Unlike the communications link applications of the THz-T technology using the same TIR emitter [18]-[19], a mechanical optical chopper [35] is employed here to modulate the radiation emitted (having a sinusoidal amplitude at a frequency of 25 Hz with the chosen disk [41]). This provides the synchronizing chopping frequency of 25 Hz required by the PIR detector [37] and its T-RAD digital radiometer [38].

C. SPECTRUM SAMPLING FILTERS

After careful consideration of COTS availability, 21 SSFs are selected to sparsely cover the 20 to 100 THz frequency range. The selected band-pass filters have measured transmittances given in Fig. 5. It can be seen that these responses are sufficient to enable sparse spectrum sampling of MUTs that are not dominated by narrow molecular absorption lines.

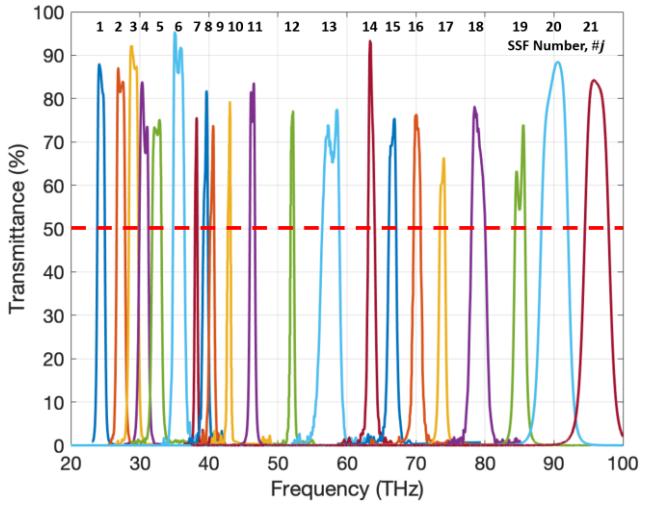

FIGURE 5. Measured transmittances for 21 COTS spectrum sampling filters. Red dashed line indicates 50% transmittance passband threshold.

A detailed specification summary for the 21 SSFs is given in Table 2, where the geometric centre frequency is $f_{0_j} = \sqrt{f_{1_j} f_{2_j}}$; f_{1_j} and f_{2_j} refer to the 50% cut-on and cut-off frequencies for the j^{th} SSF, respectively; $\mathcal{T}_{SSF_j}(f_0)$ is the transmittance at centre frequency for the j^{th} SSF. Due to the asymmetry of the passbands, $\mathcal{T}_{SSF_j}(f_0)$ represents a useful qualitative indicator. In practice, for the j^{th} SSF, the band-average transmittance $\overline{\mathcal{T}_{SSF_j}(f)}$ is a quantitatively more meaningful parameter. This can be determined from discrete measured passband values of transmittance $\mathcal{T}_{SSF_j}(f)$, with:

$$\overline{\mathcal{T}_{SSF_j}(f)} = \frac{1}{f_{2_j} - f_{1_j}} \int_{f_{1_j}}^{f_{2_j}} \mathcal{T}_{SSF_j}(f)\,.\,df \xrightarrow{\text{discrete}} \frac{1}{M_j} \sum_{i=1}^{M_j} \mathcal{T}_{SSF_j}(f) \tag{10}$$

where, M_j represents the total number of discrete measurements available between the 50% cut-on and cut-off frequencies for the j^{th} SSF; this can vary between 12 and 237 measurements, depending on the filter. The corresponding band-average insertion losses are given in Table 2.

D. BEAM COLLIMATION-FOCUSING

An analytical method was previously reported by the authors [44] for extracting a beam's cross-sectional profile and width, for a perfect Gaussian source, as illustrated in Fig. 6 for our collimated TIR beam setup.

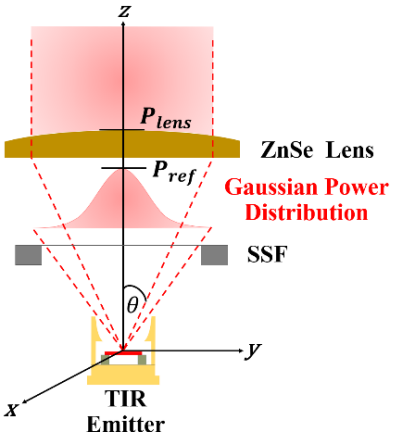

FIGURE 6. Collimated TIR beam setup with non-blocking filter.

For a Gaussian distribution, the approximation for beam power intensity (or irradiance) is given by [44]:

$$I(r) = I_o \cdot e^{-2\left(\frac{r}{w_z}\right)^2} \tag{11}$$

where, I_o is the peak beam intensity, r is the radial distance from the center axis of the beam and w_z defines the beam radius at $1/e^2 \simeq 13.5\%$ of its peak intensity (or $1/e$ of its peak field). The two-sigma (i.e., $1/e^2$ normalized power) boundary for the collimated Gaussian beam contains 95.45% of the beam power. The TIR emitter radiation is assumed to be efficiently confined by its parabolic reflector; having a $1/e^2$ angular beamwidth of ±20° at a distance of 100 mm [18], [33]. The total collimated beam width $2w_z = 2d \cdot \tan(20°) \simeq 21.8$ mm is expected at the focal point distance d =30.0 mm, as illustrated in Fig. 7.

TABLE 2. COTS spectrum sampling filter specifications from Fig. 5.

SSF Number, #j	Centre Frequency, f_{0_j} (THz)	50% Cut-on Frequency, f_{1_j}(THz)	50% Cut-off Frequency, f_{2_j} (THz)	Fractional Bandwidth, $(f_{2_j} - f_{1_j})/f_{0_j}$ (%)	$\overline{\mathcal{T}_{SSF_j}(f)}$, (%)	Band-average Insertion Loss, $-10\log_{10}\{\overline{\mathcal{T}_{SSF_j}(f)}\}$ (dB)	Substrate Material	Thickness, (mm)	Shape	Filter Size, (mm×mm) (Ø, mm)	Filter Aperture, (mm×mm) (Ø, mm)	Filter Blockage †Ø = 9 mm [18], (%)	Minimum Emitter Beam Width, (mm)	Manufacturer: NOC [34], Thorlabs [40]	Gas Absorption Line
1	24.36	23.82	24.91	4.47	76.71	1.15	Germanium	1.00	Square	5.00×5.00	4.27×4.27	71.3	9.5	NOC	-
2	27.25	26.63	27.88	4.59	74.47	1.28	Germanium	1.00	Square	4.22×4.22	3.30×3.30	82.8	7.6	NOC	-
3	29.10	28.46	29.75	4.43	81.29	0.90	Germanium	1.00	Square	5.00×5.00	4.27×4.27	71.3	9.5	NOC	NH_3
4	30.57	29.92	31.23	4.29	70.25	1.53	Germanium	1.00	Square	4.22×4.22	3.30×3.30	82.8	7.6	NOC	O_3
5	32.45	31.79	33.12	4.10	68.44	1.65	Germanium	1.00	Square	4.22×4.22	3.30×3.30	82.8	7.6	NOC	-
6	35.63	34.81	36.46	4.63	84.91	0.71	Germanium	1.00	Square	4.22×4.22	3.30×3.30	82.8	7.6	NOC	-
7	38.15	37.98	38.33	0.92	65.33	1.85	Germanium	0.60	Square	4.18×4.18	3.30×3.30	82.8	7.6	NOC	-
8	39.52	39.21	39.83	1.57	66.09	1.80	Germanium	0.65	Square	6.00×6.00	5.15×5.15	58.3	11.8	NOC	-
9	40.46	40.18	40.75	1.41	61.88	2.08	Germanium	1.00	Square	6.00×6.00	5.15×5.15	58.3	11.8	NOC	SO_2
10	42.95	42.77	43.14	0.86	64.55	1.90	Germanium	1.00	Square	6.00×6.00	5.15×5.15	58.3	11.8	NOC	H_2O
11	46.30	45.93	46.67	1.60	74.68	1.27	Germanium	1.00	Circle	25.40 Ø	23.80 Ø	No Blockage	21.8	NOC	-
12	52.05	51.82	52.29	0.90	69.17	1.60	Germ./Sapp.	0.60	Square	4.22×4.22	3.30×3.30	82.8	7.6	NOC	-
13	57.66	56.44	58.91	4.28	68.32	1.65	Sapphire	1.00	Square	5.00×5.00	4.27×4.27	71.3	9.5	NOC	NO
14	63.33	63.07	63.59	0.82	76.69	1.15	Sapphire	0.55	Square	5.20×5.20	4.55×4.55	67.4	10.4	NOC	CO
15	66.60	66.08	67.13	1.58	67.79	1.69	Sapphire	1.00	Square	5.00×5.00	4.27×4.27	71.3	9.5	NOC	N_2O
16	70.17	69.68	70.67	1.41	68.46	1.65	Sapphire	1.00	Square	6.35×6.35	5.30×5.30	55.8	12.1	NOC	CO_2
17	73.83	73.45	74.21	1.03	60.64	2.17	Alumina Oxide	1.00	Circle	25.40 Ø	23.80 Ø	No Blockage	21.8	NOC	-
18	79.05	78.14	79.97	2.31	68.97	1.61	Sapphire	0.60	Square	4.18×4.18	3.30×3.30	82.8	7.6	NOC	-
19	85.09	84.37	85.81	1.69	61.37	2.12	Fused Quartz	1.00	Circle	25.40 Ø	23.80 Ø	No Blockage	21.8	NOC	HC
20	90.08	88.22	91.98	4.17	78.78	1.04	Fused Silica	1.00	Circle	25.00 Ø	23.80 Ø	No Blockage	21.8	Thorlabs	CH_4
21	96.20	94.51	97.92	3.54	76.04	1.19	Fused Quartz	1.00	Circle	25.40 Ø	23.80 Ø	No Blockage	21.8	NOC	-

† Calculated beam blockage relative to an angular beam width of ±20 deg for a non-blocking filter located at a distance of 12.2 mm from the heated membrane inside the TIR emitter [18].

The diverging beam from the TIR emitter is collimated by a ZnSe plano-convex lens. The ZnSe lenses have a diameter and clear aperture of 25.4 mm and 20.32 mm, respectively. The centre thickness measures 3.3 mm, while the edge thickness is approximately 1.4 mm; the plano-convex lens has a 43.05 mm radius of curvature.

ZnSe lenses provide sufficient transmittance within the visible spectral range for a red laser to be used for initial beam alignment. Note that safety gloves are required when handling ZnSe, as it is a toxic material [42].

The measured transmittance responses from our previous KBr and new ZnSe lenses, as well as the reflectance response for the enhanced gold-coated mirror, and the THZ5B PIR detector absorptance are shown in Fig. 8.

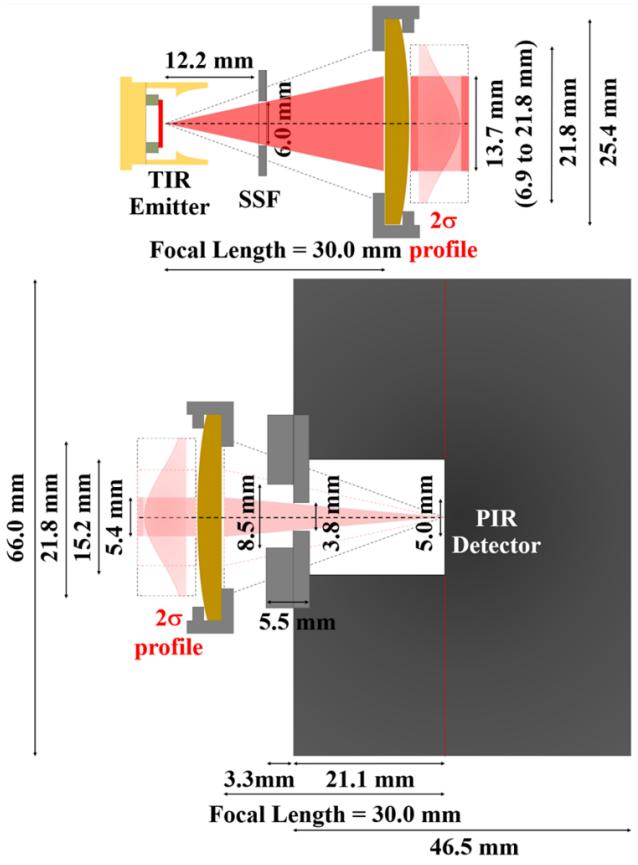

FIGURE 7. Illustrations of beam collimation and focusing at ~30 mm separation distance between emitter-to-lens (above) and lens-to-detector (below) with aperture blockage from the filter and detector, respectively.

The conformal coating applied to the KBr lens provides durability and reliability in harsh environments, although it also reduces the optical transmittance of the lens to an average of ~75% between 20 and 100 THz. It can be seen that the ZnSe lens has an improved transmittance over the same spectral range. The reflectance response for the Thorlabs's 'mid-IR enhanced protected gold mirror' is constant at 99.5% [39]. Given two identical collimating lenses, the extended size of the thermal source A_e will be projected onto the detector element plane.

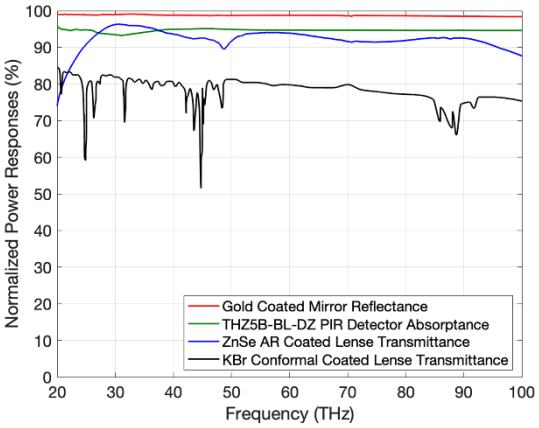

FIGURE 8. Measured normalized power responses for the mid-IR enhanced protected gold mirror [39], THZ5B-BL-DZ PIR detector [37], 25.4 mm diameter anti-reflection (AR) coated ZnSe [42] and 16.28 mm diameter conformal coated KBr lenses [36].

E. PIR DETECTOR AND T-RAD

The THZ5B-BL-DZ PIR detector (from Gentec Electro Optics Inc.) offers a wide dynamic range measurement capability, from a minimum noise equivalent power of 5 nW to a maximum average power of 20 mW, with 1 nW resolution. The PIR detector has an internal 'aperture diameter' of 5 mm. However, the default 'mechanical aperture' is 15.2 mm (with an 'aperture disk' this is reduced to 3.8 mm, with the '5B' option of our PIR detector model [37]), as illustrated in Fig. 7.

The detector has a broadband spectral sensitivity, ranging between approximately 0.1 and 1,200 THz. Gentec-EO calibrates the detector at 475 THz and provides typical frequency correction data from 0.7 to 1,200 THz [37]. Note that, up to 5 THz, absorption is below approximately 60% and, as a result, it cannot be used as a reference detector; only relative power measurements can be undertaken [46]. The absorbing layer (with our 'BL' option) has power absorptance $\mathcal{A}_D = 1 - \mathcal{R}_D$ (where $\mathcal{R}_D$ is the power reflectance at the detector element plane) spectral curves, which allows accurate power measurements to be undertaken; for example, with $\mathcal{A}_D(30\ \text{THz}) \sim 93\%$ and $\mathcal{A}_D(100\ \text{THz}) \sim 95\%$ [46].

With reference to Fig. 9, for stable readings, the 25 Hz chopping frequency (associated with the chopper's external synchronization square-wave output signal, connected directly to the T-RAD's 'EXT. TRIG.' input) must be set to 25 Hz and be within ±0.1 Hz, required for the synchronization band-pass filter (centred at 25 Hz with our 'DZ' option) [38].

The T-RAD digital radiometer has a built-in 12-bit analog-to-digital converter (ADC) and its digital signal processing (DSP) lock-in amplifier software simplifies the process of configuring the radiometer for THz measurements [38].

The square-wave signal from the chopper synchronizes the 25 Hz phased-locked loop (PLL) to produce the reference sinusoidal signal. The T-RAD implements an I-Q demodulator, using a pair of phase specific detectors (PSDs), fed with reference sine and cosine signals having an amplitude of 1 V.

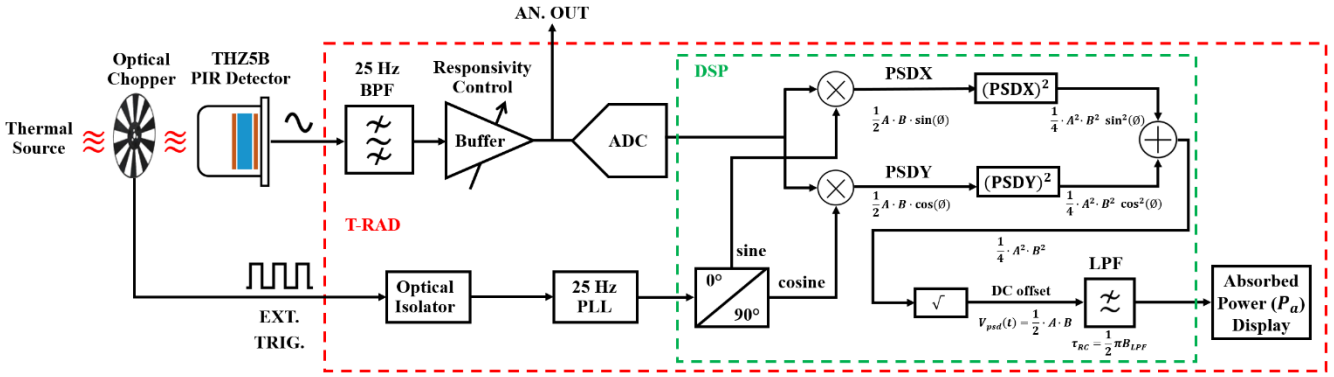

FIGURE 9. **System block diagram for the basic internal architecture of the T-RAD (based on the manufacturer's manual description [38]).**

These reference signals are multiplied by the detected 25 Hz sinusoidal signal (from the chopped TIR radiation), to frequency translate down to the zero difference frequency (DC). A low-pass filter is employed to remove the unwanted spectral component (i.e., the 50 Hz sum frequency) and to minimize unwanted noise from the detected signal. Here, the T-RAD's post-detection integration time $\tau_{RC} = 0.5\pi B_{LPF}$ (which can be set between 0.1 and 50 seconds), and displayed as the time constant 'filter tau', is kept at its default value of 1 second. With this first-order low-pass filter (used in the DSP lock-in amplifier), the 3 dB noise bandwidth is $B_{LPF} = 0.159$ Hz.

The T-RAD software can display the detector's incident power P_i or absorbed power P_a. When the THZ5B-BL-DZ PIR detector is connected, the T-RAD will automatically apply the appropriate PIR wavelength $\lambda = c/f$ correction data, based on the default 475 THz calibration of the spectral absorption (or absorptance) curve for our specific PIR detector. Alternatively, TIR wavelength correction requires additional parameters (e.g., area of the source being used, A_e, and λ_{peak}) entered for the selected power range. Again, when these parameters are entered, the power displayed is the corrected power value P_a, for any wavelength defined by Planck's law, and given as [47]:

$$Power\ Corrected\ (P_a) = Power\ Measured\ (P_i) \times Correction\ Multiplier\ (\mathcal{A}_D = P_a/P_i) \quad (12)$$

T-RAD's responsivity is the ratio of the peak amplitude for the sinusoidal output voltage (i.e., signal from the 'AN. OUT' port) to its displayed corrected power P_a. By selecting one of the 'power scales' settings, T-RAD's corresponding 'responsivity' R_v (V/W) can be changed by the buffer amplifier at a chopping frequency of 25 Hz [47]. This should not be confused with the responsivity of the detector.

IV. EXPERIMENTAL THz-T SPECTROMETERS

Photographs of the compact prototype THz-T spectrometer demonstrators, operating in both transmission and reflection modes, are shown in Figs. 10(a) and 10(b), respectively. In transmission(reflection) mode, the total path length between the TIR emitter and PIR detector is 9(12) cm. The reflection mode measurements have mirror/sample incidence and reflection angles of 45°.

Mounts for the TIR emitter, filter, optical chopper, lenses, MUT and PIR detector are 3-D printed. In addition, standard 30 mm × 30 mm aluminum alloy struts (having 6 mm slots) are mounted on optical breadboards to easily and securely adjust the transmission lengths between individual mounts. This prototyping solution gives effortless component assembly and alignment using the 'plug and play' approach we recently adopted at upper-millimetre-wave frequencies [43]; avoiding the need for a skilled operator to use cost-intensive optical aligners for individual components (which would ordinarily take many hours).

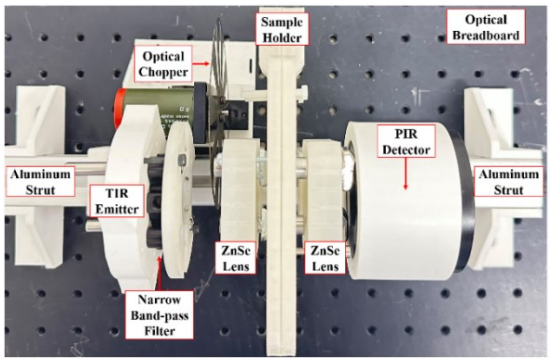

(a)

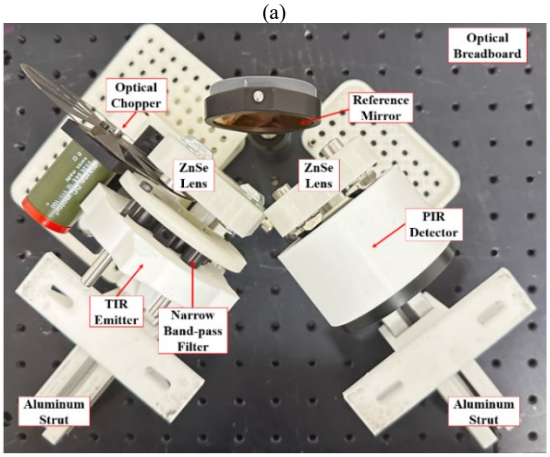

(b)

FIGURE 10. **Compact prototype THz-T spectrometer demonstrators: (a) transmission mode (empty sample holder for calibration with 3 cm lens-to-lens path length); and (b) reflection mode (sample holder replaced by the reference mirror for calibration with 3 cm lens-to-mirror path length).**

A comprehensive (but not exhaustive) analytical review of common reflection-transmission mode spectroscopy, with normal incidence of the electromagnetic wave in free space [11] (or guided-wave [48]) onto a material under test, has been previously reported by the authors.

In general, the transmittance through a material is influenced by the complex refractive index, thickness, inhomogeneity, and surface roughness (i.e., exhibiting specular and/or diffusion scattering). Similarly, reflectance from a material is affected by these factors, along with the angle of incidence and any surface coatings. Normal incidence reflection mode measurements are more cumbersome to implement, especially with (quasi-)optical systems, even though they are ideal for opaque materials under test that cannot be measured with the simpler transmission mode configuration [11].

When an electromagnetic wave is incident upon a nonopaque medium (solid, liquid or gas), some of this incident power P_i is reflected back P_r, a proportion may be absorbed P_a and the remainder transmitted through P_t; such that the principle of conservation of energy is observed at each frequency (i.e., $P_i = P_r + P_a + P_t$) [11], [17], [48]. The incident, reflected, transmitted and absorbed power (as a function of the associated electric- or E-field) can be respectively represented by $P_i(E_i)$, $P_r(E_r)$, $P_t(E_t)$, $P_a(E_a)$. The corresponding definitions for the normalized power response: (i) reflectance $\mathcal{R} = P_r/P_i = |E_r/E_i|^2$, with return loss given as $-10log_{10}\{\mathcal{R}\}$ (dB); (ii) transmittance $\mathcal{T} = P_t/P_i = |E_t/E_i|^2$, with absorbance of $1/\mathcal{T}$, or insertion loss given as $-10log_{10}\{\mathcal{T}\}$ (dB); and (iii) absorptance $\mathcal{A} = P_a/P_i$ [11], [48], with loss factor given as $-10log_{10}\{\mathcal{A}\}$ (dB).

With 21 discrete SSFs, measurements are undertaken for both the transmission and reflection modes. Transmittance is calculated by taking the ratio of measurements with and without the MUT in place. Reflectance is calculated by taking the ratio of measurements with the MUT and with a reference mirror. Absorptance is calculated using the principle of conservation of energy, where $\mathcal{A} = 1 - \mathcal{T} - \mathcal{R}$ [11], [17], [48]-[49].

V. THERMAL NOISE POWER LINK BUDGET ANLAYSIS

The thermal noise power link budget model for transmission and reflection modes can be represented by the block diagrams shown in Figs. 11(a) and 11(b), respectively. With both, $p_e(f,T)$ represents the power spectral density of the TIR emitter. Unlike with our previous work, the 50% cut-on and cut-off frequency limits are not used. This is because of the high band-average insertion losses of the SSFs within the 50% transmittance bandwidth, exhibiting significant leakage of power outside of this bandwidth. Here, the frequency range between lower frequency $f_{Lj} < f_{1j}$ and upper frequency $f_{Uj} > f_{2j}$ limits is used (taken from the original discrete measurements supplied by the filter manufacturer).

$\mathcal{T}_{SSF_j}(f)$ denotes the measured transmittance for the j^{th} SSF (having M_j discrete filter samples between f_{Lj} and f_{Uj}) that is sub-sampled every 0.1 THz, with $N_j < M_j$ discrete samples; $\mathcal{T}_{LENS}(f) \sim 92\%$ is the average transmittance (taken from the blue curve in Fig. 8) for the plano-convex anti-reflection coated ZnSe lenses; $\mathcal{T}_{REFERENCE}(f) \cong 1$ and $\mathcal{T}_{MUT_j}(f)$ are the transmittances without and with the MUT for the j^{th} SSF, respectively; $\mathcal{T}_{atm}(f)$ represents atmospheric attenuation; L_c represents frequency-independent losses (e.g., parabolic reflector losses, aperture blockages, optical misalignment and any spreading losses). This parameter can also include the absorptance of the THZ5B-BL-DZ PIR detector, which has an approximate value of 94.5% within our spectral range, as shown in Fig. 8.

As discussed in Subsection III(D), spreading losses within our THz-T system is corrected for by using collimated beams. In practice, with our implementation, aperture blockage dominates L_c. Table 1 lists the filter blockage for each SSF, at the TIR emitter end, with 82.8% being the maximum value for a uniform beam profile. However, as illustrated in Fig. 7, the 3.8 mm aperture disk blockage for our PIR detector dominates. As a result, with a Gaussian beam profile, the effective beamwidth is approximately 0.5-sigma; only ~38% of the power goes through, giving $L_c \sim 0.359$.

Similarly, $\mathcal{R}_{REFERENCE}(f) = 0.995$ and $\mathcal{R}_{MUT_j}(f)$ are the reflectances for the reference path with the mirror and with the MUT for the j^{th} SSF, respectively.

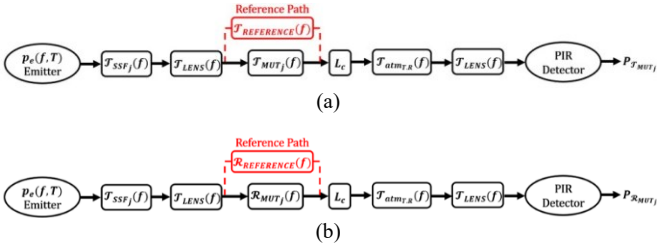

FIGURE 11. Power link budget model for the THz-T spectrometer: (a) transmission mode; and (b) reflection mode.

Atmospheric attenuation is inevitable and frequency dependent. This is referred to here as atmospheric transmittance $\mathcal{T}_{atm_{T,R}}(f)$; transmission and reflection modes are identified by the corresponding subscript letter designations *T* and *R*, respectively.

Finally, $P_{\mathcal{T}_{REFERENCE_j}}$ and $P_{\mathcal{T}_{\mathrm{MUT}_j}}$ are the absorbed power levels (measured by T-RAD), without and with the MUT in place for the j^{th} SSF, respectively. Similarly, the $P_{\mathcal{R}_{REFERENCE_j}}$ and $P_{\mathcal{R}_{MUT_j}}$ are the absorbed power levels (measured by T-RAD), with the reference mirror and with the MUT for the j^{th} SSF, respectively.

In Subsection III(B), it was shown that the model for the TIR emitter can be approximated using Planck's law, using (1) to (8). Given $\mathcal{T}_{SSF_j}(f)$ and integrating over the spectral range of

interest for each filter, for the transmission mode, the calculated absorbed power levels in the PIR detector without (13) and with (14) a MUT present are respectively given by:

$$P_{\mathcal{T}_{REFERENCE_j}} = L_c \cdot \int_{f_{L_j}}^{f_{U_j}} p_e(f,T) \cdot \mathcal{T}_{SSF_j}(f) \cdot \mathcal{T}_{LENS}^2(f) \cdot \mathcal{T}_{atm_T}(f) \cdot df \ \text{[W]} \quad (13)$$

$$P_{\mathcal{T}_{MUT_j}} = L_c \cdot \int_{f_{L_j}}^{f_{U_j}} p_e(f,T) \cdot \mathcal{T}_{SSF_j}(f) \cdot \mathcal{T}_{LENS}^2(f) \cdot \mathcal{T}_{atm_T}(f) \cdot \mathcal{T}_{MUT_j}(f) \cdot df \ \text{[W]} \quad (14)$$

where, f_{L_j}, f_{U_j} and $\mathcal{T}_{SSF_j}(f)$ are taken from Fig. 5. Similarly, for the reflection mode, the calculated absorbed power levels in the PIR detector with the reference mirror (15) and MUT (16) are given respectively by:

$$P_{\mathcal{R}_{REFERENCE_j}} = L_c \cdot \int_{f_{L_j}}^{f_{U_j}} p_e(f,T) \cdot \mathcal{T}_{SSF_j}(f) \cdot \mathcal{T}_{LENS}^2(f) \cdot \mathcal{T}_{atm_R}(f) \cdot \mathcal{R}_{REFERENCE}(f) \cdot df \ \text{[W]} \quad (15)$$

$$P_{\mathcal{R}_{MUT_j}} = L_c \cdot \int_{f_{L_j}}^{f_{U_j}} p_e(f,T) \cdot \mathcal{T}_{SSF_j}(f) \cdot \mathcal{T}_{LENS}^2(f) \cdot \mathcal{T}_{atm_R}(f) \cdot \mathcal{R}_{MUT_j}(f) \cdot df \ \text{[W]} \quad (16)$$

Atmospheric attenuation is attributed to the absorption by and scattering from air molecules, particulates and liquid droplets [17]. The HITRAN database [50] with 'HITRAN on the Web' (HoW) simulation software [51] are used to investigate molecular absorption lines with free-space propagation along line-of-sight transmission paths. HITRAN's spectroscopic parameters are often updated by improved experimental techniques, measurements and analysis. The authors previously investigated various atmospheric attenuation simulation software packages, covering the extended terahertz spectrum (i.e., from 0.1 to 100 THz) [17]. Due to its simplicity and free availability with online access, HoW is now used as standard in our THz-T systems designs.

Since only generic atmospheric attenuation needs to be considered here, a horizontally homogeneous atmospheric profile is assumed – based on the values given at sea level for the US Standard 1976 Model [51], with setting and parameter values given in Table 3.

The spectral radiance in HoW is expressed as a function of wavenumber and is weighted by the emissivity of the atmosphere at each wavenumber. Such that the emitted spectral radiance is $I = \mathcal{E} \cdot I_{BB}$, where $\mathcal{E} = \mathcal{A}$ under thermodynamic equilibrium. Absorptance is a function of frequency and physical parameters (e.g., optical path length, temperature and pressure); while I_{BB} is a function of wavenumber and temperature. Therefore, the emitted spectral radiance is dependent on all these parameters [17].

TABLE 3. 'HITRAN on the Web' user settings and parameter values.

Parameter	Value	Unit
Minimum wavenumber, WN_{min}	667	cm^{-1}
Maximum wavenumber, WN_{max}	3,336	cm^{-1}
Temperature, T	296	K
Pressure, P	1	atm
Intensity cut-off, I_{cut}	10^{-28}	cm/mol
Line shape, *Shape*	Voigt	-
Wavenumber step, WN_{step}	1	cm^{-1}
Spectral line wing length, W_{ing}	50	half-width
Optical path length, *Opt. path*	0.09 and 0.12	m
Apparatus function, *AF*	No influence of the device	-

For our applications, HoW displays the molecular absorption lines from 20 to 100 THz, with a spectral resolution of 30 GHz (corresponding to $WN_{min} = 667\ cm^{-1}$, $WN_{max} = 3{,}336\ cm^{-1}$, $WN_{step} = 0.01\ cm^{-1}$), respectively.

Path transmittance due to atmospheric attenuation for the transmission and reflection modes $\mathcal{T}_{atm_{T,R}}(f)$, using the corresponding $L_p = 90$ mm and 120 mm optical path lengths (given in Table 3), are simulated and the results shown in Fig. 12(a) and 12(b), respectively, at normal room temperature and pressure. As expected, absorption lines are more pronounced with the 33% increase in path length.

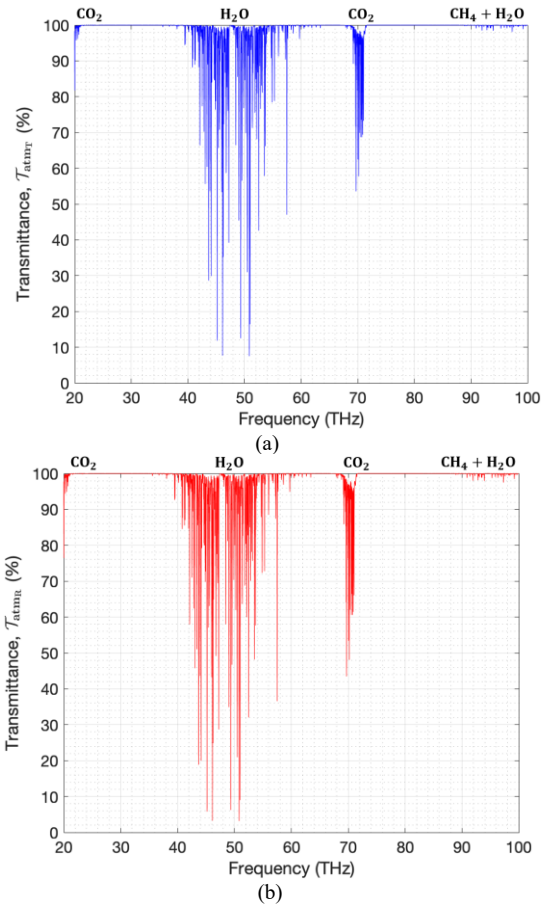

FIGURE 12. Predicted free-space atmospheric transmittances against frequency from 'HITRAN on the Web': (a) transmission mode with path length L_p = 90 mm; and (b) reflection mode with path length L_p = 120 mm.

The effects from carbon dioxide (CO_2) can be seen at ~21 and ~70 THz. The atmospheric contribution of gaseous water vapor (H_2O) can also be seen with both path lengths, at frequencies between approximately 42 to 57 THz. Methane (CH_4) and gaseous water vapor have little effects over our two path lengths between 90 and 100 THz. Contributions from other molecular species over our spectral range of interest are insignificant when compared to those from gaseous water vapor and carbon dioxide [17].

The authors previously reported several generic approaches for calculating mean channel transmittance (MCT); this represents a useful figure-of-merit for quantifying a path's resilience to atmospheric attenuation (e.g., for communications link applications [17]-[19]). An accurate definition for MCT, introduced by Hang *et al.* [18]-[19] in 2020, is adopted here to represent the mean path transmittance calculated for each SSF with our THz-T spectrometer:

$$\mathcal{T}_{path_j}(T, L_p) = \frac{\int_{f_{Lj}}^{f_{Uj}} p_e(f,\ T) \cdot \mathcal{T}_{SSF_j}(f) \cdot \mathcal{T}_{atm_{T.R}}(f,\ L_p) \cdot df}{\int_{f_{Lj}}^{f_{Uj}} p_e(f,\ T) \cdot \mathcal{T}_{SSF_j}(f) \cdot df} \quad (17)$$

All the SSFs employed in this THz-T system have excellent mean path transmittance values; with predicted worst-case values being above 87%, as shown in Fig. 13. The atmospheric attenuation from gaseous water vapour influences SSFs #8 to #13; while CO_2 only influences SSF #16.

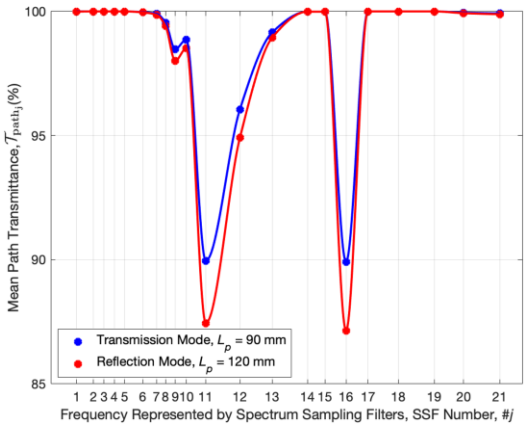

FIGURE 13. Predicted THz-T spectrometer mean path transmittance for each SSF, using (17), at normal room temperature and pressure.

Figure 14 shows the predicted THz-T spectrometer reference power performances for each SSF. Figure 14(a) gives the absorbed power in the PIR detector, calculated using (13) and (15) for the transmission and reflection modes, respectively. Figure 14(b) shows the corresponding dynamic range, relative to the minimum noise equivalent power level of 5 nW for our PIR detector. It can be seen that our prototype THz-T spectrometer has a minimum dynamic range of 42.5 dB, which is dictated by our filter #9 (due the lowest level of power passing through the filter). This level of dynamic range is sufficient for characterizing a MUT with a broad range of dielectric properties.

Finally, using (13) to (16), the predicted THz-T spectrometer's transmittance and reflectance spectra can be expressed as:

$$\mathcal{T}_{THz-T_j} = \frac{P_{\mathcal{T}_{MUT_j}}}{P_{\mathcal{T}_{REFERENCE_j}}} \xrightarrow{ideally} \mathcal{T}_{MUT_j} \quad (18)$$

$$\mathcal{R}_{THz-T_j} = \frac{P_{\mathcal{R}_{MUT_j}}}{P_{\mathcal{R}_{REFERENCE_j}}} \xrightarrow{ideally} \mathcal{R}_{MUT_j} \quad (19)$$

Given high-resolution validation measurements (or simulations) for the MUT [11], for high-to-low-conversion predictions, the corresponding values for $\mathcal{T}_{MUT_j}$ and $\mathcal{R}_{MUT_j}$ are inserted into (14) and (16), respectively. The system's absorptance $\mathcal{A}_{THz-T_j}$ can then be determined by applying the principle of conservation of energy, such that:

$$\mathcal{A}_{THz-T_j} = 1 - \mathcal{T}_{\mathrm{THz-Tj}} - \mathcal{R}_{THz-T_j} \quad (20)$$

Using (18) to (20), with our THz-T spectrometer, an inhouse database for different MUTs can be created; ideally these spectra will be close to (but not exactly the same as) those from commercial spectrometers.

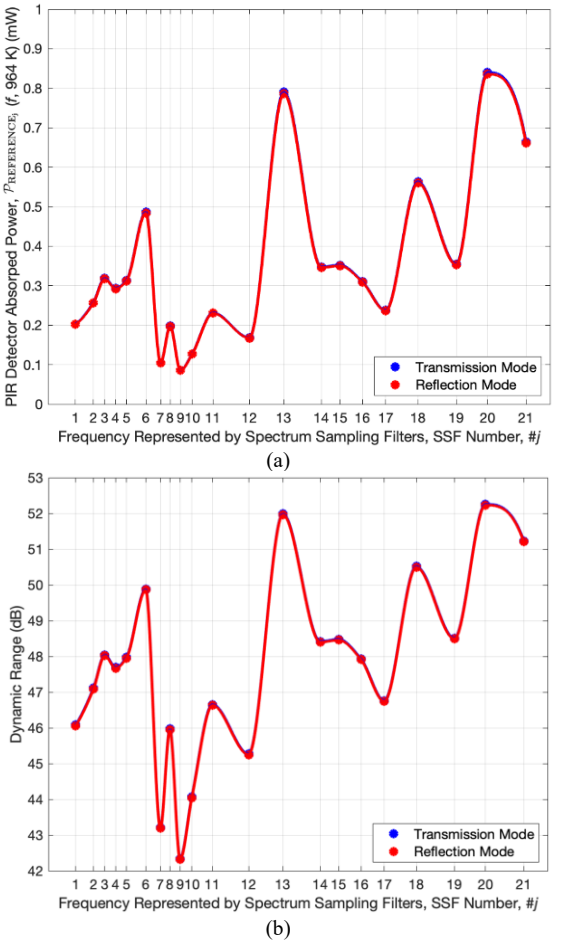

FIGURE 14. Predicted THz-T spectrometer reference power performances for each SSF: (a) absorbed power in the PIR detector; and (b) dynamic range.

VI. THz-T SPECTROMETER MEASURMENTS

A. MATERIAL SELECTION

To evaluate the performance of our experimental prototype THz-T spectrometer, benchmarking measurements using commercial high-end research grade (space-domain interferometer-based) systems are undertaken for a broad selection of traceable materials under test, exhibiting different spectral signatures. Table 4 details the chosen materials used and their physical parameters.

For the high-resolution validating transmittance measurements, two instruments are employed: Bruker VERTEX 80v FTIR spectrometer [52], at Cardiff University, having a spectral resolution of 116 GHz; and Nicolet 5700 FTIR, at Imperial College London, having a spectral resolution of 58 GHz [53]. For the high-resolution validating reflectance measurements, only one instrument is employed: HYPERION 3000 FTIR microscope [54], at Cardiff University, having a spectral resolution of 231 GHz.

As with the SSFs, the original MUT validation measurements (having V_j discrete spectral samples between f_{Lj} and f_{Uj}) are re-sampled every 0.1 THz with $N_j \neq V_j$ discrete samples; ensuring compatibility with (13) and (17).

With any MUT, three measurements are taken and averaged for each SSF. Each measurement is spaced at intervals of 1 to 60 seconds, until the PIR's absorbed power displayed has stabilized within the T-Rad software; while also allowing sufficient time to manually read-off the data. In practice, there is relatively little change in the three measured values. While this process is inefficient, accuracy was prioritized over speed with our proof-of-concept experiments. With a fully-automated system, data acquisition time could be dramatically speed-up.

Prior to any measurements, the experimental setup is first calibrated (within the T-Rad software), based on the TIR emitter temperature; previously discussed in Subsection III(B). All MUT measurements are conducted within a laboratory environment at normal room temperature, shrouded with black curtains (mitigating against potential interference from other infrared radiation sources).

Reproducibility for any spectrometer measurements is based on time-varying conditions (e.g., stability of the source, optical alignment, detector sensitivity and environmental influences). Our THz-T system has the advantages of not having cryogenic cooling, a vacuum chamber or highly-sensitive interferometry. As an example, the original banknote measurements using the common SSFs, undertaken in 2015 [20], are almost indistinguishable from those presented in this paper; presented in Subsection VI(B).

Materials formed with simple molecules generally have infrared spectral signatures that exhibit smooth features. A broad range of material samples are characterized in this work, starting with simple glasses. The dominant component in our glass-like materials is silicon dioxide (SiO_2). Here, as a baseline reference, two fused SiO_2 wafers are measured: fused quartz (JGS2) [55] and fused silica (Hoya) [56]. It should be noted that fused silica is sometimes also referred to as fused quartz or quartz glass; representing an amorphous version of quartz crystal. Unlike crystalline quartz, fused silica lacks long-range crystalline order [57].

The Japanese Glass Standard (JGS) with number '2' indicates a specific subcategory, under the Japanese Industrial Standards (JIS) system [58]. Other JGS glass subcategories (e.g., JGS1, JGS3, JGS4, etc.) have distinct optical properties and applications. JGS2 has a transmittance of ~90%, above 150 THz within the near-infrared and within visible spectrum.

TABLE 4. Traceable material under test specifications

Material Category	Material Under Test	Sample Size (mm×mm) (Ø, mm)	Sample Thickness (μm)	Wafer (Y/N)	Optically Polished (Y/N)	High-resolution Measurements		Ref.
						Transmittance (Y/N)	Reflectance (Y/N)	
Silicon Dioxide, SiO_2	Fused Quartz (JGS2)	102 Ø	500	Y	Y	Y†	Y†	[44], [55]
	Fused Silica (Hoya)			Y	Y	Y†	Y†	[44], [56]
Glass	Borosilicate Glass (SuperEpoxy 2)	25×76	1,000	N	Y	Y†	Y†	[44], [59]
Silicon <100>	N-type LRS ($5-10\ \Omega \cdot cm$)	100 Ø	500	Y	Y	Y†	Y†	[60]
Semi-insulating, GaAs	Undoped GaAs (100)	76 Ø	640	Y	Y	Y⸸	N	[61]
Ceramic	Alumina, Al_2O_3	26×26	630	N	N	Y†	Y†	-
Polymer	polyimide film (Kapton®)	25×56	25	N	N	Y†	Y†	[62]
	Polytetrafluoroethylene, PTFE (Teflon™)	100×100	1,500	N	N	Y⸸	N	[63]
			2,000	N	N	Y⸸	N	[63]
	Polypropylene, PP		3,000	N	N	Y⸸	N	[64]
	GBP Banknote	139×73	100	N	N	Y⸸	N	[65]
	CAD Banknote	52×70		N	N	Y†	Y†	[66]
Cotton Paper	GBP Banknote	149×80		N	N	Y†	Y†	[67]
	CNY Banknote	155×77		N	N	Y†	Y†	[68]

† Measured at the University of Cardiff and ⸸ Measured at Imperial College London.

JGS2 glass is extensively used for optical components (e.g., lenses, prisms, windows and optical filters), mainly due to its exceptional transparency within the visible spectrum. For example, it exhibits a relatively low refractive index of ~1.46 [55], while maintaining chemical and thermal stability. The third sample consists of a 1,000 μm thick borosilicate glass (SuperEpoxy 2) [59].

Another material category of interest is traceable semiconductor wafers: N-type phosphorus-doped low resistivity silicon (LRS) [60] and undoped high resistivity gallium arsenide (GaAs) [61]; the latter used in thermal infrared optics and photonics. Also, one traceable ceramic (alumina, Al_2O_3) is chosen and this is polished on both sides. Various polymers have been selected: thin-film polyimide [62], sheet polytetrafluoroethylene [63] and sheet polypropylene [64]. Moreover, two new polymer-based banknotes are included: GBP £20 [65] and CAD $10 [66]. Finally, two cotton paper banknotes have been chosen: old GBP £20 [67] and current CNY ¥100 [68].

B. MATERIAL CHARACTERIZATION

From the 13 different materials listed in Table 4, Figs. 16(a) to 16(l) show the measured normalized power responses, obtained from: commercial high-resolution FTIR spectrometers; high-to-low conversion model predictions for our THz-T spectrometer; and our experimental prototype THz-T spectrometer demonstrator.

From the outset, since the commercial systems used can be considered as industry standard, and fully calibrated, it is assumed here that all of their high-resolution measurements are spectroscopically accurate; represent our benchmark results from which to compare the model predictions and experimental measurements. With regards to the former, which employs measurements from the commercial spectrometers, the low-resolution output sample values represent the averaging effect within the bandwidth of the j^{th} SSF, defined within (13) to (16). It can be seen that there is an almost exact match between the commercial and modeled normalised power responses.

However, when comparing the modeled and experimental results, against one another, discrepancies can be seen. For example, if measurement data for all 14 samples are combined together and the percentage differences are considered, the following is found: (i) with 294 transmittance measurements, the absolute error (worst-case difference) is ~6%; (ii) with 189 reflectance measurements, the worst-case difference (absolute error) is ~10%; (iii) with 189 absorptance measurements, the worst-case difference (absolute error) is ~17%. By combining transmittance, reflectance and absorptance, the mean values of absolute error are ~1%. Clearly, our experimental THz-T spectrometer demonstrator measurements compare well with those predicted using our modeled THz-T spectrometer.

C. MATERIAL SPECTRAL SIGNIATURES

The measured normalized power responses for the glass-like materials are shown in Figs. 16(a) to 16(c), representing fused quartz (JGS2), fused silica (Hoya) and borosilicate glass (SuperEpoxy 2), respectively. Here, it can be seen that below 60 THz, these samples are opaque and have similar (but not identical) reflectance/absorptance signatures. Above 60 THz, the samples have similar (but not identical) transmittance/absorptance signatures.

Figures 16(d) and 16(e) show the normalized power responses for the LRS and GaAs wafers, respectively. Neither semiconducting sample has any strong spectral features within the thermal infrared. As expected, the latter exhibits a spectrally flat transmittance of ~55%, across our spectral range of interest. Figure 16(f) shows that alumina is an excellent absorber between 30 and 100 THz, having an absorptance >98%.

Figures 16(g) and 16(j) represent different polymers. Due to their complex molecular structures, they inherently all have complex spectral signatures within the TIR's 'fingerprint region'. In the TIR's 'diagnostic region', between 49 to 53 THz, all the polymers exhibit an absorption peak (and corresponding transmittance dip), due to a strong intensity carbon-oxygen resonance (C=O molecular bond stretching) [69]-[70]. Similarly, between 81 to 99 THz, there is an absorption peak (and corresponding transmittance dip), due to a medium intensity carbon-hydrogen resonance (C-H molecular bond stretching) [69]-[70]. From Fig. 16(h), the PTFE and PP samples have different spectral signatures, due to their respective carbon-fluorine (C-F) and carbon-hydrogen molecular bonds [71]. From Figs. 16(i) and 16(j), both polymer banknotes have similar spectral signatures, while also sharing similar features with the polyimide sample.

Figures 16(k) and 16(l) correspond to the paper banknotes. Similar to alumina, both banknotes are almost perfectly absorbing across the whole spectral range of interest, exhibiting an absorptance of >99%.

In summary, all three glass-like samples, both semiconductor wafers, the ceramic plate and both paper banknotes have relatively simple spectral signatures within the thermal infrared. As a result, our THz-T spectrometer is ideally suited for measuring these material categories. With regards to the polymer-based MUTs (which include two different banknotes), the spectral signatures are complicated, due to the wide range of molecular resonances. Nevertheless, our THz-T spectrometer can still identify broadband absorption features.

VII. DISCUSSION AND CONCLUSION

In this study, our experimental THz-T spectrometer is investigated for the first time in detail. A comprehensive description of the basic system is given, which includes the TIR emitter, SSFs, beam collimation-focusing components, PIR detector and T-Rad digital radiometer. From this, a thermal noise power link budget model is given for both transmission and reflection modes of operation, which includes atmospheric attenuation, mean path transmittance for each SSF and predicted THz-T spectrometer power performances. This study benchmarks our experimental THz-T spectrometer demonstrator against high-resolution commercial FTIR spectrometers, for a range of material categories. Our THz-T spectrometer has the capability for identifying MUTs with smooth spectral signatures.

This article has been accepted for publication in IEEE Access. This is the author's version which has not been fully edited and
content may change prior to final publication. Citation information: DOI 10.1109/ACCESS.2024.3359054

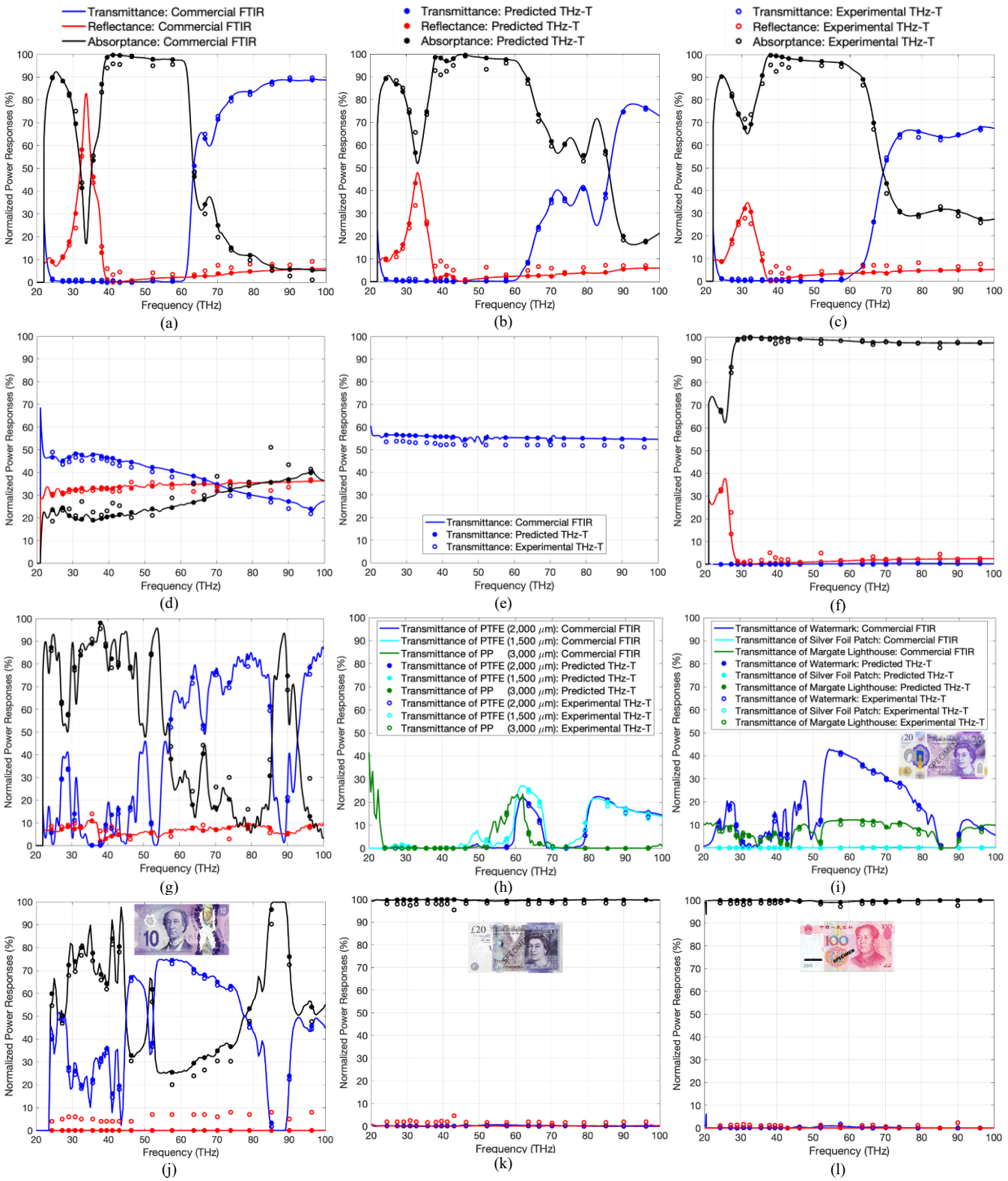

FIGURE 16. Normalized power measurements from: commercial high-resolution FTIR spectrometers (solid lines); high-to-low conversion model predictions of our THz-T spectrometer (solid fill circular markers); and experimental prototype THz-T spectrometer demonstrator (no fill circular markers): (a) fused quartz (JGS2); (b) fused silica (Hoya); (c) borosilicate glass (SuperEpoxy 2); (d) low-resistivity silicon; (e) high-resistivity GaAs; (f) alumina; (g) polyimide (Kapton®); (h) PTFE (Teflon™) and PP; (i) polymer GBP £20 banknote; (j) polymer CAD $10 banknote; (k) cotton paper GBP £20 banknote; and (l) cotton paper CNY ¥100 banknote. Unless otherwise stated, the legend at the top of the figure is used (i.e., (a) to (g), (j) to (l)).

With our prototype demonstrator, the measured performance in transmission mode closely matches the predicted results from our modeled THz-T spectrometer, for all 14 chosen MUT samples. However, small discrepancies have been found in the reflection mode, which can be attributed to two reasons. First, with the use of the commercial FTIR microscope (for high-resolution reflectance measurements), systematic errors are introduced with changes in the focal plane position relative to the MUT's surface. Second, for reasons of layout convenience, our THz-T spectrometer reflectance measurements have a fixed 45° angle of incident, which may result in a small degree of angular misalignment.

It is important to state that the primary objective for our THz-T spectrometer is material identification/classification and not to provide spectroscopically accurate results (associated with commercial FTIRs). To this end, a database of previously characterized MUTs is created using sparse frequency spectrum sampling.

To address the inherently low SNR, found with non-TDS systems, statistical methods and machine learning algorithms [19] can be introduced for accurate material identification. In addition, aperture disk blockage (at our PIR detector) dominates and so when removed more power will be detected, thus, also increasing the dynamic range of our system. Moreover, increasing the number of SSFs will enhance the capability for identifying materials having more complex spectral signatures.

To justify the low-cost nature of our prototype THz-T spectrometer, we avoid the use of expensive cryogenic cooling and interferometry. Moreover, unlike the commercial systems that we used for benchmarking, our THz-T spectrometer does not use an expensive vacuum chamber for housing the MUTs. In addition, our spectrometer only employs COTS components that have been mounted in very-low cost 3D-printed assemblies. For example, the FTIR Bruker VERTEX80v spectrometer costs in the region of £100k-120k (for the base unit only). A dedicated THz mercury-vapour lamp costs approximately £10k; a liquid nitrogen cooled HgCdTe infrared detector costs approximately £10k, and can achieve wavenumbers down to 600 cm^{-1} (18 THz), while a longer wavelength liquid helium cooled THz bolometer costs approximately £60k. As a result, a complete FTIR system may cost in the region of £200k-250k; comparable to a laser-based THz-TDS system. By comparison, our prototype THz-T spectrometer employs the following COTS components: (i) TIR emitter costing approximately £100; (ii) each filter costs between £200-£370 (approximately £6k in total for all 21 filters); optical chopper costs less than £1k; ZnSe lenses cost £280 each; the terahertz radiometer with PIR detector costs £2.5k; optical breadboard costs £250; while all other components can be 3D-printer very cheaply. In total, we estimate the maximum total cost of our prototype THz-T spectrometer to be less than £11k. While our individual COTS components are all sourced cheaply, economies of scale would facilitate a dramatic reduction in THz-T spectrometer price per unit, when scaled-up with commercial production.

Furthermore, the cost for implementing the THz-T spectrometer can be greatly reduced by replacing the THZ5B-BL-DZ PIR detector with a cheap ubiquitous motion-sensor PIR detector, as employed in our previous work on communication-links [12]-[19]. Moreover, the T-Rad can be replaced by a bespoke lock-in amplifier solution.

Our compact thermal infrared THz-T spectrometer offers several advantages, over commercial systems, which include hardware simplicity and low cost. In addition, it can operate in both transmission and reflection modes, utilizing the same source and detector; minimizing the number of optical components.

In contrast to conventional spectroscopy, the THz-T spectrometer has low spectral resolution and dynamic range. Nevertheless, this technology is ideal for the low cost-low performance application space – which includes non-destructive testing and non-invasive material characterization, material identification from a pre-characterized database, process variation monitoring and potentially even gas sensing.

ACKNOWLEDGMENT

The authors would like to thank Dr M. Bailey at Northumbria Optical Coatings Ltd (U.K.) for the kind donation of some of the narrow band-pass filters (Table 2) and associated measured data (Fig. 5). In addition, we would also like to thank the following people from Imperial College London: Dr S.-H. Shin (Department of Electrical and Electronic Engineering) for 3D printing the THz-T set up components; A. Baubaid (Department of Chemical Engineering) for undertaking validation measurements using his high-resolution FTIR spectrometer; and Dr Christos Papavassiliou (Department of Electrical and Electronic Engineering) for discussions on the lock-in detector.

REFERENCES

[1] THzDB. (2024). *Terahertz Spectroscopy Database*. Accessed: Jan. 13, 2024. [Online]. Available: http://www.thzdb.org/.

[2] National Research Council. "Assessment of Millimeter-Wave and Terahertz Technology for Detection and Identification of Concealed Explosives and Weapons,". Washington, DC, USA: The National Academies Press, 2007.

[3] TeraView. (2024). *Terahertz Time-Domain Spectroscopy*. Accessed: Jan. 13, 2024. [Online]. Available: https://teraview.com/.

[4] Hubner Photonics. (2024). *Terahertz Technology*. Accessed: Jan. 13, 2024. [Online]. Available: https://hubner-photonics.com/.

[5] Toptica. (2024). *Terahertz Systems: Time Domain*. Accessed: Accessed: Jan. 13, 2024. [Online]. Available: https://www.toptica.com.

[6] Laser Focus World. (2024). *Industry-grade Terahertz Time-domain Spectroscopy System has Kilohertz Measurement Rates*. Accessed: Jan. 13, 2024. [Online]. Available: https://www.laserfocusworld.com.

[7] Thermo Fisher Scientific Inc. (2024). *Nicolet iS50 FTIR Spectrometer*. Accessed: Jan. 13, 2024. [Online]. Available: https://www.thermofisher.com/order/catalog/product/912A0760?SID=srch-srp-912A0760.

[8] Agilent Technologies Inc. (2024). *FTIR - Fourier Transform Infrared Spectroscopy*. Accessed: Jan. 13, 2024. [Online]. Available: https://www.agilent.com/en/product/molecular-spectroscopy/ftir spectroscopy.

[9] Shimadzu Inc. (2024). *FTIR - Fourier Transform Infrared Spectroscopy*. Accessed: Jan. 13, 2024. [Online]. Available: https://www.ssi.shimadzu.com/products/molecularspectroscopy/ftir/index.html.

[10] Bruker Inc. (2024). *Routine FT-IR Spectrometers*. Accessed: Jan. 13, 2024. [Online]. Available: https://www.bruker.com/en/products-and-solutions/infrared-and-raman/ft-ir-routine-spectrometer.html.

[11] J. Sun and S. Lucyszyn, "Extracting complex dielectric properties from reflection-transmission mode spectroscopy," *IEEE Access*, vol. 6, no. 1, pp. 8302-8321, Jan. 2018.

[12] S. Lucyszyn, H. Lu, and F. Hu, "Ultra-low cost THz short-range wireless link," *IEEE International Microwave Workshop Series on Millimeter Wave Integrated Technologies (IMWS 2011)*, Sitges, Spain, pp. 49-52, Sep. 2011.

[13] X. Liang, F. Hu, Y. Yan, and S. Lucyszyn, "Secure thermal infrared communications using engineered blackbody radiation," *Scientific Reports,* Nature Publishing Group, Sci. Rep. 4, 5245, pp. 1-7, Jun. 2014.

[14] F. Hu and S. Lucyszyn, "Modelling miniature incandescent light bulbs for thermal infrared 'THz Torch' applications," *Journal of Infrared, Millimeter, and Terahertz Waves*, Springer, vol. 36, no. 4, pp. 350-367, Apr. 2015.

[15] F. Hu, J. Sun, H. E. Brindley, X. Liang, and S. Lucyszyn, "Systems analysis for thermal infrared 'THz Torch' applications," *Journal of Infrared, Millimeter, and Terahertz Waves*, Springer, vol. 36, no. 5, pp. 474-495, May 2015.

[16] F. Hu and S. Lucyszyn, "Advances in front-end enabling technologies for thermal infrared 'THz Torch' wireless communications," *Journal of Infrared, Millimeter, and Terahertz Waves*, vol. 37, no. 9, pp. 881-893, May 2016.

[17] J. Sun, F. Hu, and S. Lucyszyn, "Predicting atmospheric attenuation under pristine conditions between 0.1 and 100 THz," *IEEE Access*, vol. 4, pp. 9377-9399, Nov. 2016.

[18] H. Ren and S. Lucyszyn, "Thermodynamics-based cognitive demodulation for 'THz Torch' wireless communications links," *Scientific Reports*, Nature Publishing Group, Sci. Rep. 10, 6259, pp. 1-12, Apr. 2020.

[19] H. Ren, S.-H. Shin, and S. Lucyszyn, "Enhanced cognitive demodulation with artificial intelligence," *Scientific Reports*, Nature Publishing Group, Sci. Rep. 10, 20298, pp. 1-16, Nov. 2020.

[20] J. Sun, F. Hu, Z. Wang, and S. Lucyszyn, "Banknote characterization using a thermal infrared 'THz Torch' spectrometer," *Asia-Pacific Microwave Conference (APMC 2015)*, Nanjing, China, Dec. 2015.

[21] R. Risoluti, M. Fabiano, G. Gallica, S. Ciprioti, and S. Materazzi, "FTIR-evolved gas analysis in recent thermoanalytical investigations," *Applied Spectroscopy Reviews*, vol. 52, no. 1, pp. 39-72, 28, July. 2016.

[22] D. Henry, J. Watson, and C. John, "Assessing and calibrating the ATR-FTIR approach as a carbonate rock characterization tool," *Sedimentary Geology*, vol. 347, pp. 36-52, Jan. 2017.

[23] J. Xu, K. Thomas, Z. Luo, and A. Gowen, "FTIR and Raman imaging for microplastics analysis: State of the art, challenges and prospects," *TrAC Trends in Analytical Chemistry*, vol. 119, 115629, pp. 1-11, Oct. 2019.

[24] C. Kraus *et al*., "Adaptation and engine validation of an FTIR exhaust gas analysis method for C1-based potential GHG-neutral synthetic fuels/gasoline-blends containing dimethyl carbonate and methyl formate," *SAE Technical Paper*, pp. 1-23, Mar. 2022.

[25] B. O'Callahan *et al*., "In liquid infrared scattering scanning near field optical microscopy for chemical and biological nanoimaging", *Nano Letters*, vol. 20, pp. 4497-4504, May. 2020.

[26] F. Souza *et al*., "Near-field infrared microscopy: A novel analytic mapping technique to nanocharacterize calcium silicate-based cement materials," *Cement and Concrete Research*, vol. 147, 106525, pp. 1-9, Jun. 2021.

[27] U. Karst, "Analytical Chemistry: A Modern Approach to Analytical Science," ChemPhysChem, vol. 6, no. 11, pp. 750-801, 2005.

[28] Thermo Fisher Scientific Inc. (2024). *IR Microscopes*. Accessed: Jan. 13, 2024. [Online].Available: https://www.thermofisher.com.

[29] Bruker Inc. (2024). *FT-IR Microscopes*. Accessed: Jan. 13, 2024. [Online]. Available: https://www.bruker.com/en/products-and-solutions/infrared-and-raman/ft-ir-microscopes.html.

[30] Shimadzu Inc. (2024). *Infrared Microscopes*. Accessed: Jan. 13, 2024. [Online]. Available: https://www.ssi.shimadzu.com/products/ftir/ftir-spectroscopy/aimsight/index.html.

[31] PerkinElmer Inc. (2024). *FTIR Microscopy & Imaging*. Accessed: Jan. 13, 2024. [Online]. Available: https://www.perkinelmer.com/category/ftir-microscopy-imaging-instruments.

[32] Agilent Technologies Inc. (2024). *Routine FT-IR Spectrometers*. Accessed: Jan. 13, 2024. [Online]. Available: https://www.agilent.com/en/product/molecular-spectroscopy/ftir-spectroscopy/ftir-microscopes-imaging-systems.

[33] Intex Inc. (2024). *Silicon MEMS Optical Technology*. Accessed: Jan. 13, 2024. [Online]. Available: http://www.eot.it/pdf/IntexBrochure.pdf.

[34] Northumbria Optical Coatings Inc. (2024). *Narrow Band Pass Filters*. Accessed: Jan. 13, 2024. [Online]. Available: https://www.noc-ltd.com/catalogue.

[35] Bentham Inc. (2024). *Optical Chopper & Control Module*. Accessed: Jan. 13, 2024. [Online]. Available: https://www.bentham.co.uk/.

[36] Korth Kristalle Inc. (2024). *Potassium Bromide (KBr)*. Accessed: Jan. 13, 2024. [Online]. Available: https://www.korth.de/en/.

[37] Gentec-EO Inc. (2024). *THz Detectors*. Accessed: Jan. 13, 2024. [Online]. Available: https://www.gentec-eo.com/products?type=thz.

[38] Gentec-EO Inc. (2024). *T-Rad*. Accessed: Jan. 13, 2024. [Online]. https://www.gentec-eo.com/products/t-rad.

[39] Thorlabs Inc. (2024). *Mid-Infrared Enhanced Protected Gold Mirrors*. Accessed: Jan. 13, 2024. [Online]. Available: https://www.thorlabs.com/newgrouppage9.cfm?objectgroup_id=1217.

[40] Thorlabs Inc. (2024). *IR Hard-Coated Band-pass Filters*. Accessed: Jan. 13, 2024. [Online]. Available: https://www.thorlabs.com/newgrouppage9.cfm?objectgroup_id=587.

[41] Scitec Instruments Ltd. (2024). *Rotating Optical Chopper*. Accessed: Jan. 13, 2024. [Online]. Available: https://scitec.uk.com.

[42] Korth Kristalle Inc. (2024). *Zinc Selenide*. Accessed: Jan. 13, 2024. [Online]. Available: https://www.crystran.co.uk/lenses/zinc-selenide-positive-lenses.

[43] S.-H. Shin, R. Payapulli, L. Zhu, M. Stanley, X. Shang, N. M. Ridler, and S. Lucyszyn, "3-D printed plug and play prototyping for low-cost sub-THz subsystems," *IEEE Access*, vol. 10, pp. 41708-41719, Apr. 2022.

[44] S.-H. Shin and S. Lucyszyn, "Benchmarking a commercial (sub-)THz focal plane array against a custom-built millimetre-wave single-pixel camera," *IEEE Access*, vol. 8, pp. 191174-191190, Oct. 2020.

[45] High-resolution spectral modelling. (2024). *Calculating Blackbody Radiance*. Accessed: Jan. 13, 2024. [Online]. Available: https://www.spectralcalc.com.

[46] Gentec-EO Inc. (2024). *Highest Calibration Standards*. Accessed: Jan. 13, 2024. [Online]. Available: https://downloads.gentec-eo.com/prod/d476ef6e/Gentec-EO_HW_Calibration_2022_V1.1.pdf.

[47] Gentec-EO Inc. (2024). *Technical Note*. Accessed: Jan. 13, 2024. [Online]. Available: https://downloads.gentec-eo.com/prod/0089a78c/AN_202184B_Calibration_Certificate.pdf.

[48] J. Sun, A. Dawood, W. J. Otter, N. M. Ridler, and S. Lucyszyn, "Microwave characterization of low-loss FDM 3-D printed ABS with dielectric-filled metal-pipe rectangular waveguide spectroscopy," *IEEE Access*, vol. 7, pp. 95455–95486, Jul. 2019.

[49] M. Rubin, "Optical properties of soda lime silica glasses," *Solar Energy Materials.*, vol. 12, no. 4, pp. 275-288, Sep./Oct. 1985.

[50] L. S. Rothman *et al*. "The HITRAN2012 molecular spectroscopic database," *J. Quant. Spectrosc. Radiat. Transf.*, vol. 130, pp. 4–50, Nov. 2013.

[51] HITRAN On The Web. (2024). Accessed: Jan. 13, 2024. [Online]. Available: http://hitran.iao.ru/.

[52] Bruker Inc. (2024). *FT-IR Spectrometers VERTEX 80/80v*. Accessed: Jan. 13, 2024. [Online]. Available: https://www.bruker.com/en/products-and-solutions/infrared-and-raman/ft-ir-research-spectrometers/vertex-research-ft-ir-spectrometer/vertex-80-80v-ft-ir-spectrometer.html.

[53] Thermo Fisher Scientific Inc. (2024). *FTIR Spectrometer Nicolet 5700* . Accessed: Jan. 13, 2024. [Online]. Available: https://anff-q.org.au/wp-content/uploads/2016/07/Vibrational-Spectroscopy-Suite-FTIR-NICOLET-5700.pdf.

[54] Bruker Inc. (2024). *HYPERION 3000 FTIR*. Accessed: Jan. 13, 2024. [Online]. Available: https://www.bruker.com/products/infrared-near-infrared-and-raman-spectroscopy/ft-ir-microscopes-raman-microscopes/hyperion/overview.html.

[55] Microchemical Inc. (2024). *Production and Specifications of Fused Quartz Wafers.* Accessed: Jan. 13, 2024. [Online]. Available:

https://www.microchemicals.com/technical_information/fused_silica_wafers.pdf.
[56] Hoyaoptics Inc. (2024). Accessed: Jan. 13, 2024. [Online]. Available: http://www.hoyaoptics.com/specialty_glass/fused_silica.htm.
[57] Kopp Glass Inc. (2024). *Glass Transforming Light.* Accessed: Jan. 13, 2024. [Online]. Available: http://www.koppglass.com/blog/3-common-glass-types-properties applications/.
[58] Japanese Industrial Standards Committee. (2024). Accessed: Jan. 13, 2024. [Online]. Available: https://www.jisc.go.jp/eng/.
[59] Arrayit Inc. (2024). *SuperEpoxy Microarray Substrates.* Accessed: Jan. 13, 2024. [Online]. Available: https://shop.arrayit.com/microarray-epoxy-slide.aspx.
[60] HELITEK Inc. (2024). Accessed: Jan. 13, 2024. [Online]. Available: https://www.waferworks.com/en/us/helitek-company-ltd.
[61] Wafer Technology Ltd. (2024). *GaAs - Gallium Arsenide*. Accessed: Jan. 13, 2024. [Online]. Available: http://www.wafertech.co.uk/products/gallium-arsenide-gaas/.
[62] TapeCase Ltd. (2024). *Dupont™ Kapton®*. Accessed: Jan. 13, 2024. [Online]. Available: https://www.tapecase.com/products/dupont-khn-1-1-mil-kapton-film-with-no-adhesive/1-50-khn-1.
[63] Guarniflon®. (2024). *PTFE Sheets*. Accessed: Jan. 13, 2024. [Online]. Available: https://www.guarniflon.com/en/products/ptfe-sheets/skived-ptfe-sheets.
[64] Direct Plastics Ltd. (2024). *Polypropylene*. Accessed: Jan. 13, 2024. [Online]. Available: https://www.directplastics.co.uk/polypropylene-sheet.
[65] Bank of England. (2024). *£20 Notes*. Accessed: Jan. 13, 2024. [Online]. Available: https://www.bankofengland.co.uk/banknotes/polymer-20-pound-note.
[66] Bank of Canada. (2024). *$10 Polymer Note*. Accessed: Jan. 13, 2024. [Online]. Available: https://www.bankofcanada.ca/banknotes/bank-note-series/frontiers/10-polymer-note/.
[67] Bank of England. (2024). *£20 Series F*. Accessed: Jan. 13, 2024. [Online]. Available: https://www.bankofengland.co.uk/banknotes/withdrawn-banknotes.
[68] Bank of China. (2024). Accessed: Jan. 13, 2024. [Online]. Available: https://www.bankofchina.com/.
[69] LibreTexts™ Chemistry. (2024). *Infrared Spectroscopy Absorption Table*. Accessed: Jan. 13, 2024. [Online]. Available: https://chem.libretexts.org/Ancillary_Materials/Reference/Reference_Tables/Spectroscopic_Reference_Tables/Infrared_Spectroscopy_Absorption_Table.
[70] WebSpectra. (2024). *Table of IR Absorptions*. Accessed: Jan. 13, 2024. [Online]. Available: https://webspectra.chem.ucla.edu/irtable.html.
[71] Infrared Spectroscopy. (2024). *Polymer Identification Using Mid Infrared Spectroscopy*. Accessed: Jan. 13, 2024. [Online]. Available: https://resources.perkinelmer.com/labsolutions/resources/docs/app_polymeridentificationmidinfaredspectroscopy.pdf.

SALEH KOMIES (Graduate Student Member, IEEE) received the B.Eng. degree in electrical and electronics engineering from Heriot-Watt University, Edinburgh, U.K., in 2014, and the M.Sc. degree in Mobile Communication in 2015. He is currently pursuing the Ph.D. degree within the Department of Electrical and Electronic Engineering at Imperial College London. His research interests include electromagnetic for reservoir characterization, terahertz and thermal infrared technologies, and their applications.

Jingye Sun received the B.Eng. degree in electronic and electrical engineering from University College London, London, U.K., in 2012, and the M.Sc. degree in electrical and electronic engineering from Imperial College London, London, U. K., in 2013. She received the Ph.D. degree in electrical and electronic engineering from Imperial College London in 2018. She is currently an associate professor in school of electronic and information engineering, Beijing Jiaotong University, Beijing, China. Her main research interests are in terahertz metamaterial sensors and functional devices, 2D graphene devices and terahertz and thermal infrared technologies.

STEPHEN A. LYNCH (Senior Member, IEEE) received the B.Sc. (Hons) degree from University College Dublin in 1995, and the Ph.D. degree from Trinity College Dublin in 2000, for his work on the optoelectronic properties of self-pulsating semiconductor lasers. Following postdoctoral positions at the Cavendish Laboratory, Cambridge, and the London Centre of Nanotechnology, University College London, he moved to Cardiff University where he is currently Professor of Physics in the School of Physics and Astronomy, and Dean of Research and Innovation for the College of Physical Sciences and Engineering. His research explores how electromagnetic radiation, including ultraviolet, visible, infrared, and THz light, interacts with matter on timescales from picoseconds to milliseconds. He has made contributions to the development of THz SiGe quantum cascade lasers, and to the quantum optics of atomic impurities in single crystal silicon and diamond. Other interests include the physics of photocatalysis in titanium dioxide. His current EPSRC funded research explores the fascinating quantum phenomenon of excitons in cuprous oxide.

CHRIS HODGES is a research associate, in the School of Physics and Astronomy with the Condensed Matter and Photonics Group at Cardiff University. His research interests include optical spectroscopy and semiconductor physics.

JONATHAN S. WATSON received B.Sc. in Geology from University of Edinburgh (1994), M.Sc. in Petroleum Geochemistry (1995) and Ph.D. in Organic Geochemistry (1999) both from University of Newcastle-upon-Tyne. He is currently a Research Officer in Organic Geochemistry and Mineralogy with the Imperial College Organic Geochemistry group in the Department of Earth Science and Engineering. Research interests include meteorites & extraterrestrial organic matter and organic proxies of environmental change.

STEPAN LUCYSZYN (Fellow, IEEE) received the Ph.D. degree in electronic engineering from King's College London, University of London, London, U.K., in 1992, and the D.Sc. degree (Hons.) in millimetre-wave and terahertz electronics from Imperial College London, London, in 2010.

He is currently a Professor of millimetre-wave systems with Imperial College London. He has coauthored well over 200 articles and 12 book chapters in applied physics and electronic engineering. In 2005, he was made a fellow of the Institution of Electrical Engineers, U.K., and the Institute of Physics, U.K.. In 2008, he became a fellow of the Electromagnetics Academy, USA. He was elected a fellow of the Royal Academy of Engineering, U.K., in 2023. He was appointed as an IEEE Distinguished Microwave Lecturer, from 2010 to 2013. He co-founded the Imperial College London spin-out company Drayson Wireless Ltd., in 2014. In 2022, for their work on 3D printing, Lucyszyn and his team at Imperial College London won Junkosha's inaugural Technology Innovator of the Year Award for the Microwave and Millimeter Wave category.